

# 銅銦鎵硒薄膜太陽能電池中關鍵吸收層的濺鍍 硒化製程技術優化

學生：江濟宇

指導教授：謝漢萍教授

國立交通大學電機學院

光電工程研究所

## 摘要

銅銦鎵硒是一種具有潛力的薄膜太陽能電池材料。在此論文中針對硒化製程中的附著度，均勻的鎵分佈和緻密的表面做研究。首先論文中提出了一種適合硒化法的成長路徑，經由二元相的討論，提出了三種不同的成長路徑，分別由  $\text{Cu}_{2-x}\text{Se}$ 、 $\beta\text{-In}_2\text{Se}_3$  和  $\text{Cu}_{2-x}\text{Se}$  及  $\beta\text{-In}_2\text{Se}_3$ 。經由此研究結果發現由  $\text{Cu}_{2-x}\text{Se}$  及  $\beta\text{-In}_2\text{Se}_3$ ，所生成的銅銦鎵具有附著性佳和緻密的表面，更進一步的提出了三階段的製程。在鎵分佈方面，提出了四階段退火，來解決鎵在銅銦鎵硒中分佈不均的問題。在此研究結果中，先以  $125^\circ\text{C}$  預熱，再以  $350^\circ\text{C}$ 、 $450^\circ\text{C}$  和  $550^\circ\text{C}$  的退火，具有最佳化的結果，所生成的銅銦鎵具有附著性佳、緻密的表面、高強度比值的  $(220/204)/(112)$  和較均勻的鎵分佈。

# The absorber fabrication by sputtering and selenization processes in $\text{Cu}(\text{In,Ga})\text{Se}_2$ thin film solar cells

Student: Chi-Yu Chiang

Advisor: Dr. Han-Ping D. Shieh

Dept. of Photonics & Institute of Electro-Optical Engineering  
National Chiao Tung University

## Abstract

Thin film solar cells with Copper Indium Gallium Diselenide ( CIGS ) absorber layers are one of the most promising candidates to emerge as an efficient solar cell technology in the near future. The aim of this thesis is to develop a fabrication method for the CIGS absorber with densely-packed, well adhered, and uniform Ga depth-profiled properties by sputtering and selenization processes. Firstly, the growing mechanism of  $\text{CuInSe}_2$  (CIS) films by using sputtered precursor films and selenization process was presented. Three dominant growing paths of selenized CIS films, including  $\text{Cu}_{2-x}\text{Se}$ ,  $\beta\text{-In}_2\text{Se}_3$ , and  $\text{Cu}_{2-x}\text{Se}/\beta\text{-In}_2\text{Se}_3$  binary compounds paths, were determined by

analyzing Cu-Se and In-Se binaries. The CIS films with the  $\text{Cu}_{2-x}\text{Se}/\beta\text{-In}_2\text{Se}_3$  growing path exhibited relatively uniform and larger grain size in surface morphology. As a result, a well-defined formation path for CIS-based chalcopyrite films with three-step annealing process was achieved. Moreover, a four-step annealing process consisting of pre-heating treatment and followed annealing at elevated temperatures was studied to improve the depth-profiled Ga distribution of CIGS films. The pre-heating of the sputtered Cu-Ga-In and evaporated Se film was utilized to mitigate the adhesion and Ga accumulation issues in the formation of CIGS films. The optimized annealing temperatures were 125°C in preheating procedure, 350°C, 450°C, and 550°C in the followed annealing processes, respectively. In this study, resulting films with four-step annealing exhibited large-grained, and 112/220/204-orientation chalcopyrite CIGS phase, as well as smooth depth-profiled distribution in the Ga concentration.

## Contents

Chapter 1 .....	1
Introduction .....	1
1-1. Photovoltaic technology .....	1
1-2. Cu(In,Ga)Se <sub>2</sub> thin film solar cells .....	5
Chapter 2 .....	8
CuIn <sub>1-x</sub> Ga <sub>x</sub> Se <sub>2</sub> .....	8
2-1. CIGS solar cells structure .....	8
2-2. Fundamental aspects of the material .....	11
2-3. Phase Diagram .....	11
2-4. Defects and Impurities .....	15
2-5. Band gap of various compounds .....	17
2-6. High-Efficiency Techniques .....	18
2-7. CIGS absorber layer fabrication .....	21
2-8. Motivations .....	24
Chapter 3 .....	26
Experimental .....	26
3-1. CIGS deposition system .....	26
3-2. Analytical technologies .....	33
Chapter 4 .....	40
Results and discussion .....	40



4-1. Cu-Se phase .....	40
4-2. In-Se phase.....	43
4-3. Cu-In-Se phase.....	48
4-4. Growing paths determination .....	52
4-5. Cu-In-Ga-Se phase.....	55
4-6. Three step process .....	57
4-7. Four step process .....	63
4-8. Comparison.....	67
Chapter 5.....	69
Conclusions and future works.....	69
5-1. Conclusions .....	69
5-2. Future works .....	70
References .....	73

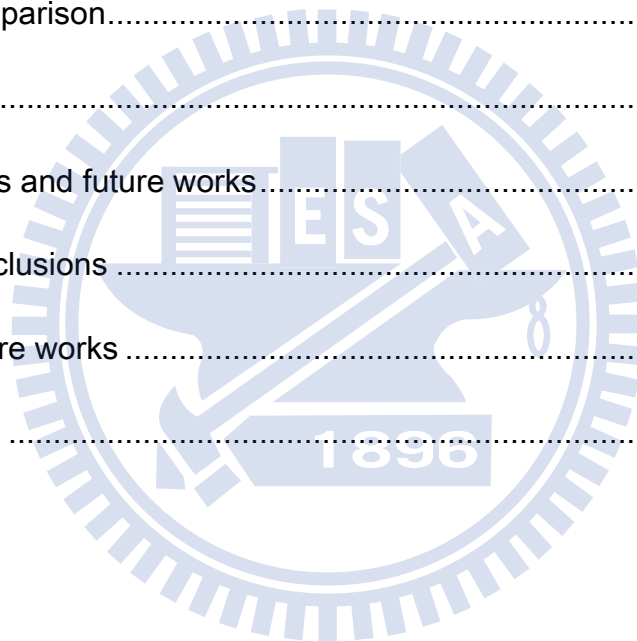


## Figure Captions

Fig. 1-1 Classification of solar cells.....	2
Fig. 1-2 Cost/efficiency domains for the three generations of photovoltaic technology. ....	2
Fig. 1-3 Absorption Coefficients of Various Semiconductor Materials. ....	5
Fig. 1-4 The best laboratory cell efficiencies for solar cell (standard conditions). ....	7
Fig. 2-1 A structure of CIGS solar cells.....	8
Fig. 2-2 Simplified version of ternary phase diagram.....	12
Fig. 2-3 Pseudobinary cut $\text{Cu}_2\text{Se-In}_2\text{Se}_3$ of ternary phase diagram in Fig. 1-6. ....	13
Fig. 2-4 Crystal growth and change of the phases in the CIGS films.....	15
Fig. 2-5 Energy band gap of various semiconductor.....	18
Fig. 2-6 CIGS thin-film solar cells as a function of Cu/III ratio.....	20
Fig. 2-7 Bandgap profiling of CIGS solar cell.....	20
Fig. 2-8 Schematic of co-evaporation method. ....	22
Fig. 2-9 Three-stage process.....	23
Fig. 2-10 Illustration of selenization process.....	24
Fig. 3-1 Schematic of NCTU deposition system. ....	26

Fig. 3-2 NCTU sputter system. ....	27
Fig. 3-3 Schematic of sputter. ....	29
Fig. 3-4 NCTU selenization system. ....	30
Fig. 3-5 Schematic of evaporation. ....	31
Fig. 3-6 Schematic of SEM. ....	34
Fig. 3-7 SEM at NCTU. ....	34
Fig. 3-8 Schematic of XRD. ....	37
Fig. 3-9 XRD at National Device Laboratory. ....	37
Fig. 3-10 Schematic of RS. ....	38
Fig. 3-11 Raman at Nano Facility Center (NFC), NCTU. ....	39
Fig. 4-1 The SEM surface morphology of Cu-Se binary compound. ....	41
Fig. 4-2 Cu-Se XRD in different temperature. ....	43
Fig. 4-3 The SEM surface morphology of In-Se binary compound annealed at (a) RT, (b) 150°C, (c) 250°C, (d) 300°C, (e) 350°C, (f) 450°C, and (g) 550°C. ....	44
Fig. 4-4 In-Se XRD annealed in different temperature. ....	46
Fig. 4-5 In-Se raman annealed in different temperature. ....	46
Fig. 4-6 Fig. 4-6 The SEM cross-section of Cu-In-Se annealed at (a) 250°C, (b) 350°C, (c) 450°C, and (d) 550°C. ....	49

Fig. 4-7 Cu-In-Se XRD annealed in different temperature. ....	50
Fig. 4-8 Cu-In-Se Raman annealed in different temperature. ....	50
Fig. 4-9 SEM micrographs of CIS films prepared with (a) path 1, (b) path 2, and (c) path 3.....	52
Fig. 4-10 SEM micrographs of CIS films prepared with (a) path 1, (b) path 2, and (c) path 3.....	54
Fig. 4-11 (a) XRD scans and (b) Raman spectra of CIS films selenized with three paths. ....	54
Fig. 4-12 SEM micrographs of CIGS prepared with path 3 by co-sputtering (a) Top-view and (b) cross-section.. ....	56
Fig. 4-13 Raman scans of three-step annealing CIGS films annealed of (a) 350°C, (b) 450°C, and (c) 550°C.....	60
Fig. 4-14 XRD of the three step processed CIGS.....	61
Fig. 4-15 SEM micrographs of CIGS prepared with three three step process (a) Top-view and (b) cross-section.....	61
Fig. 4-16 The modified structure.....	61
Fig. 4-17 SEM micrographs of CIGS prepared with Ga solution(a) Top-view and (b) cross-section.....	63

Fig. 4-18 Cross-sectional SEM micrographs of CIGS films with (a) three-step and (b) four-step annealing process. .... 64

Fig. 4-19 Depth-profiled Ga/(In+Ga) ratio through the bulk of CIGS film prepared by three- and four-step annealing processes. .... 66

Fig. 4-20 The band diagram of (a) three- and (b) four-step processes ... 66

Fig. 5-1 The schematic explanation of the first-step process. .... 71

Fig. 5-2 The fabrication process of double-stacked precursors and followed selenization..... 71

Fig. 5-3 Raman shift of the CIGS film after the first annealing. .... 72



## List of Tables

Table 1-1 Comparison thin-film solar cells.....	5
Table 4-1 Cu-Se EDS analyses.....	42
Table 4-2 In-Se EDS analyses.....	45
Table 4-3 Cu-In-Se cross-EDS results.....	49
Table.4-4 Standard Free Energies , $G^\circ$ , of Some Compounds Relevant to the Mo/CIGS/CdS/ZnO System.....	57
Table 4-5 Top view EDS analyses.....	60
Table 4-6 Cross-view EDS analyses for three step annealing.....	60
Table 4-7 Top view EDS analyses.....	62
Table 4-8 Cross section view EDS analyses for Ga solution.....	62
Table 4-9 Top view EDS analyses.....	65
Table 4-10 Cross-sectional EDS analyses [Ga/(In+Ga) ratio].....	65
Table 4-11 Comparisons of two methods .....	68

# Chapter 1

## Introduction

Most of our energy supply comes from coal, oil, natural gas, or nucleus, and they are not immediately replaced. Therefore the development of clean energy resource as alternative to non-renewable energy is becoming one of the most important challenges for technologies.

Among the wide variety of renewable energy projects in development, photo -voltaic (PV) shows the great potential to be the next generation devices. Thin film PV modules are the next evolutionary step towards cost-effective generation of electricity from sunlight. Thin film copper indium gallium diselenide (CIGS) solar cells have been established as a leading contender to achieve cost-effective generation of electricity from sunlight.

### ***1-1. Photovoltaic technology***

The first solid-state PV device was demonstrated in 1877 and consisted of a rod of selenium held between two wire electrodes [1]. The PV effect is based on which a PV cell converts sunlight into electricity. Photovoltaics is a semiconductor technology that silently converts light energy into direct-current (DC) electricity. Currently, Photovoltaic technologies can be divided into three generations with different materials, as shown in Figs. 1-1 and 1-2.

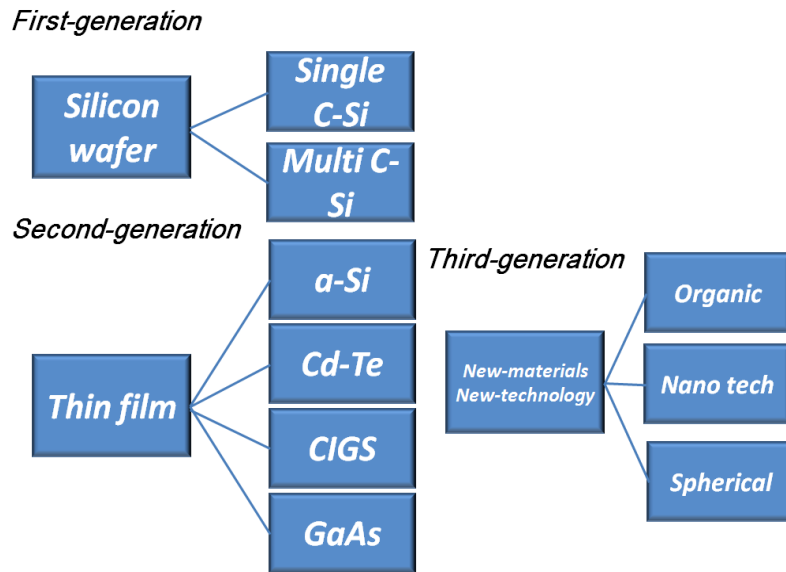


Fig. 1-1 Classification of solar cells.

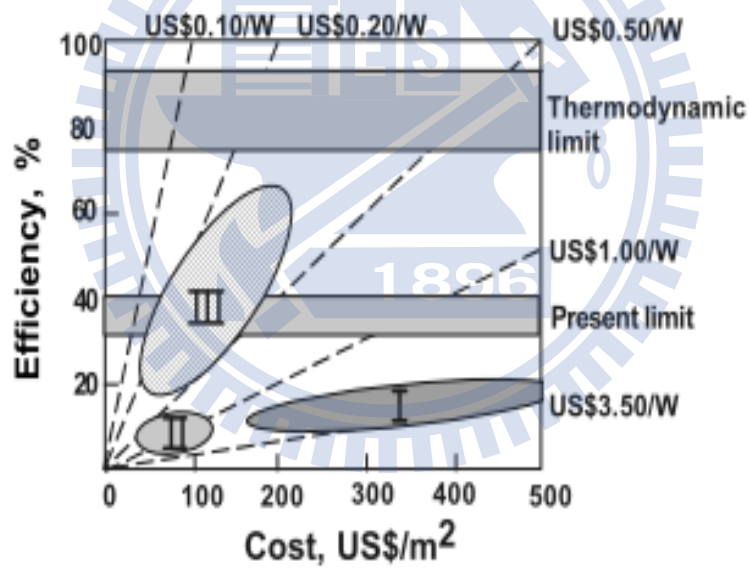


Fig. 1-2 Cost/efficiency domains for the three generations of photovoltaic technology: (I) wafer-based;(II) thin-film; and (III) high-efficiency thin-film.

The first generation is the wafer-based crystalline silicon solar technology, which was the material used in the first successful solar devices and still popular nowadays. Single-crystalline and multi-crystalline solar cells are matured technologies that have achieved cell efficiencies to around 25% and



20%, respectively [2-3]. However, due to its indirect band gap and low absorption coefficient properties, adequate thickness is required to collect sufficient sunlight. Therefore, although wafer-based silicon solar cells can produce such high efficiency, high material cost and substrate-limitation constricted its application and commercial value.

To overcome the issues of crystalline silicon solar cells, high absorption materials and thin film devices, which belong to the second generation one, were researched. The film-thickness of the absorber in thin film solar cells was of less than  $10\mu\text{m}$ , which was obviously thinner than that of crystalline silicon as more than  $100\mu\text{m}$ . As a result, thin film solar cells with low material cost were adapted to inexpensive substrates such as glass, flexible plastic, and stainless steel.

Compared to previous technology, the third generation requires the properties not only low cost and thin film approaches but also high conversion efficiency to offset unavoidable area-related material and installation costs. The main criteria for such “third-generation” technology was that it has efficiency potential beyond that of a single junction cell, in thin-film form to maintain low area costs and use abundant, non-toxic, robust and durable materials so that the technology can be widely deployed without environmental concerns. Robustness is a key requirement since, to reach the low costs indicated in Fig. 1-2 encapsulation costs will need to be considerably reduced from those of “first-generation” Silicon wafer-based modules. Even

though such cells are notably robust, present encapsulation costs are estimated as at least US\$90/m<sup>2</sup>. Therefore, in the years to come, thin film is one of the promising candidates because of the reasons discussed below. Amorphous silicon (a-Si), copper indium diselenide (CIS or CuInSe<sub>2</sub>), and cadmium telluride (CdTe) are main semiconductor materials used in thin film solar cells. Fig. 1-3 shows the absorption coefficient for the semiconductor materials. Among these materials, CIS shows the relative high absorptivity, which means that 99% of the incident light will be absorbed within the first micrometer of the film. Moreover, the band gap of CIS material can be raised from 1.0 to 1.7eV by doping small amounts of Gallium to the CIS film. The raise of the band gap improves the theoretical conversion efficiency in CIS solar cells. The solid solution of gallium into CIS material forms chalcogenic Cu(In,Ga)Se<sub>2</sub> (CIGS) compounds, which has a raised band gap of 1.3~1.4. Table 1-1 shows the comparison of the thin film technologies. Till now, CIGS can achieve 20.3% in cell efficiency and 13.8% in module efficiency, which is relatively higher than the others. Therefore, the chalcogenic CIGS absorber has the potential to be the next generation solar technology, which shows low production cost, high conversion efficiency, and cadmium-free capability.

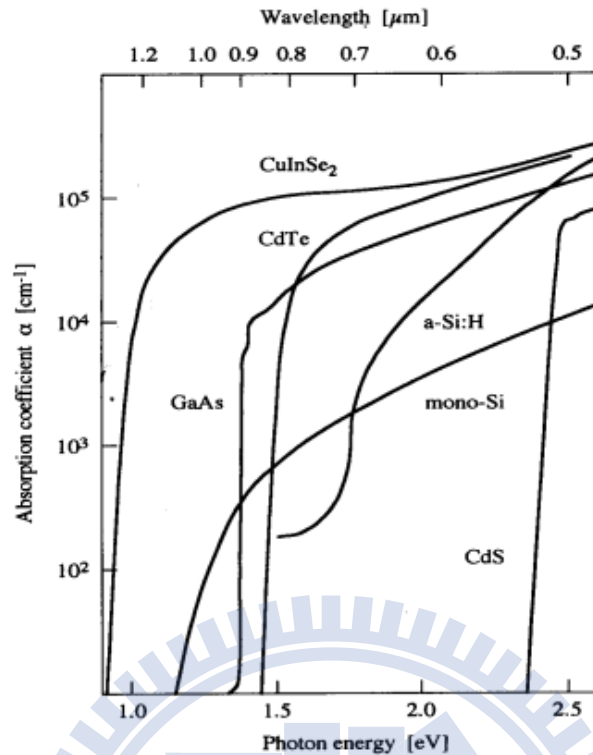


Fig. 1-3 Absorption coefficients of various semiconductor materials.

Table 1-1 Comparison thin-film solar cells.

	a-Si	Cd-Te	CIGS
Junction	Triple-junction	Single-junction	Single-junction
Cell efficiency	15%	16.7%	20.3%(ZSW)
Module efficiency (corporation)	7% (Kaneka)	11.6% (First Solar)	13.8% (Showa)
Cost	US\$1.3/Wp	US\$0.75/Wp	????
Process	PECVD	Close spaced sublimation	Co-Evaporation/ selenization
Vacuum process	Yes	Yes	Yes or No

## 1-2. *Cu(In,Ga)Se<sub>2</sub> thin film solar cells*

The creation of the first CIS PV device was demonstrated in 1973, when a research team at Salford University annealed a single crystal of the ternary compound semiconductor  $\text{CuInSe}_2$  in indium [4]. In the recent years, the cell

efficiency of the CIGS solar cell has approached 20.3% under standard test conditions in laboratory-scale devices, as well as 13.8% in module [23]. On the other hand, the best laboratory-reported efficiency of wafer-based crystalline silicon solar cells was about 20% [3]. It indicates that the cell efficiency of CIGS thin-film technology can be as high as the best efficiency in wafer-based crystalline silicon solar cell. However, the potential of CIGS has not yet been fully exploited. As a multinary compound, it behaves different characteristics than conventional semiconductor materials. From the very beginning of research, CIGS has showed superiority among all thin-film technologies with respect to solar cell efficiencies as shown in Fig. 1-4. Almost all subsequent CIS thin-film deposition process development for PV device applications have sought to make the compound  $\text{CuInSe}_2$  or alloys thereof, in fact, generally result in a multiphase mixture [5], incorporating small amounts of other phases. Therefore, manufacturability has always been an issue. Future development must show to what degree presently available thin-film technologies will make CIGS competitive in the large-scale production of photovoltaics.

# Best Research-Cell Efficiencies

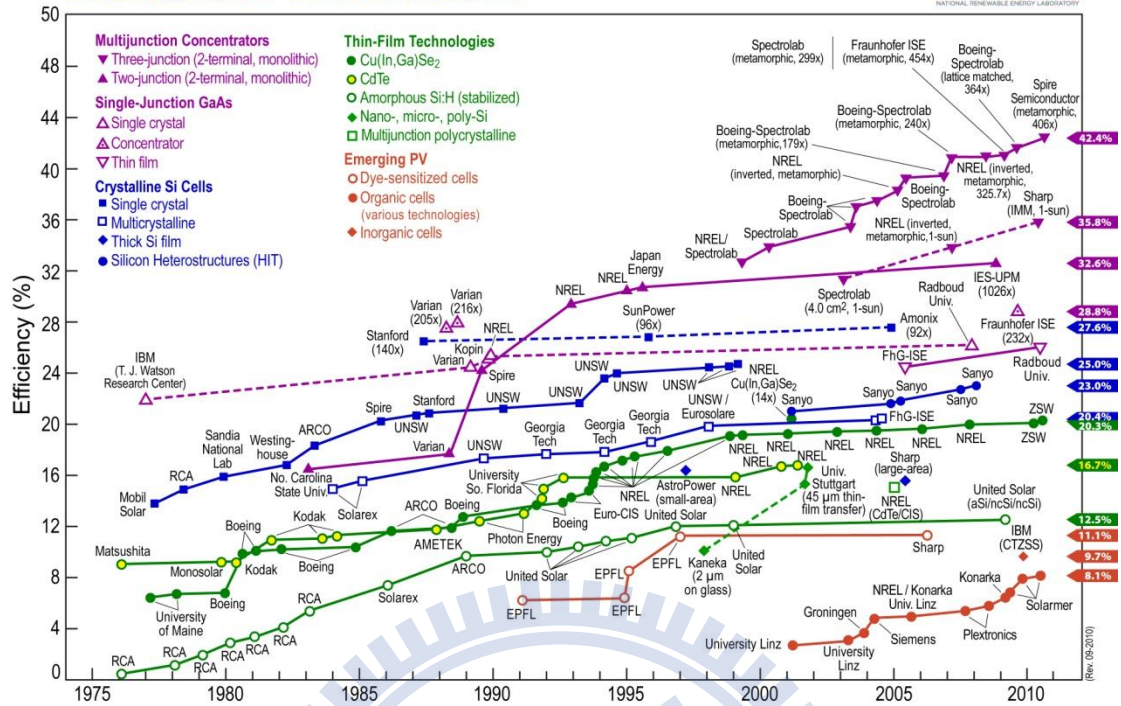


Fig. 1-4 The best laboratory cell efficiencies for solar cell (standard conditions) published by National Renewable Energy Laboratory (NREL).

# Chapter 2

## $\text{CuIn}_{1-x}\text{Ga}_x\text{Se}_2$

### 2-1. CIGS solar cells structure

A typical structure of CIGS solar cells is shown in Fig. 2-1. The fabrication of the CIGS solar cell starts with the deposition of back contact molybdenum (Mo) on substrates, followed by CIGS absorber, buffer layer (usually CdS or ZnS), window layer (i-ZnO & AZO), and the front contact Aluminum.



Fig. 2-1 A structure of CIGS solar cells.

### Substrate

In CIGS thin-film solar cells, soda lime glass (SLG) is widely used as a substrate. It is reported that the Na diffusion from the soda lime substrate into the CIGS film enhances the grain growth of the absorber layer and is also effective to increase the hole-concentration. Besides, Na also can be intentionally doped by using  $\text{Na}_2\text{O}_2$ ,  $\text{Na}_2\text{S}$ ,  $\text{Na}_2\text{Se}$ , and  $\text{NaF}$  compounds. Small amount of Na (0.1 at%) in the CIGS formation process was found to increase hole concentration to about  $10^{20} \text{ cm}^{-3}$  [6].

## **Back contact metal**

The back contact metal is the back electrode of the CIGS solar cells. Several materials were reported to be the contact metal [7-8]. A typical back contact metal is Mo. In addition, during the CIGS formation procedure at high temperature, Mo would interact with Se to form an extremely thin MoSe<sub>2</sub> layer in the interface of Mo and CIGS layers. The formation of MoSe<sub>2</sub> were reported to benefit the solar device performance as MoSe<sub>2</sub> results in the ohmic contact, and would not cause the losses of short-circuit current (J<sub>sc</sub>) [9].

## **CIGS absorber layer**

The absorber layer is the most important layer in the CIGS solar cell device and will be discussed in sections 2-2 to 2-6 for material properties and 2-7 for fabrication process, respectively.

## **Buffer layer**

The CdS films deposited by chemical bath deposition (CBD) process are widely used as an interfacial layer of the CIGS thin film solar cells in order to improve the efficiency. The role of the CBD-CdS buffer layer is a prevention of undesirable shunt paths through the portion of the very thin CdS buffer layer and the protection of the junction region from sputtering damage during subsequent transparent conducting oxide (TCO) deposition. Recently, several research groups reported that the diffusion of Cd into the CIGS absorber and the formation of a junction inside the absorber [11]. Wada et al. reported that

when CIGS films were soaked in the  $\text{Cd}^{2+}$  aqueous solution, Cd atoms were doped in the CIGS surface by the substitution of Cu atoms in the CIGS films by Cd ions in the solution. SIMS depth-profile analyses clearly demonstrated that the Cd concentration is the highest at the CIGS surface and it decreases into the CIGS films. The Cd concentration reached the background level at a depth of about 20 nm. The CBD-ZnS also shows the same result, and the Zn atoms were doped in the CIGS surface by the substitution of Cu atoms in the CIGS films by Zn ions in the solution.

### **i-ZnO**

A high resistivity ZnO layer eliminated the CdS-related absorption losses and the current-leakage path. The open-circuit voltage and fill factor of the device are significantly dependent on the resistivity of i-ZnO layer.

### **Window layer**

The name of window layer derives from the function of acting as window, letting the photon coming inside to the absorber layer. The main functions of the window layer are: (1) the transmittance of light to the CIGS absorber region, (2) the transmittance of the photocurrent with the lowest ohmic losses, and (3) reduction of the surface recombination. For the low cost material, aluminum-doped zinc oxide (AZO) shows the potential. Typical deposition technique for the window layer is sputtering.



## ***2-2. Fundamental aspects of the material***

Many elements in CIGS solar cells can form a great variety of compounds during cell processing; therefore, the CIGS system is very complicated. On the other hand, CIGS is tolerant to defect and impurity because of the chemistry, as well as the structure, can adjust itself in many possible ways [14-15]. Fortunately, this adjustment generally occurs in the way that is favorable to photovoltaic properties. A high level of performance of the solar cells in the laboratory and in pilot production of modules has been achieved on an intuitive basis and by empirical optimization of the deposition process and device. The issues now are how far we can get with this development, how we can get closer to the theoretical limit, and whether there is an intrinsic mechanism that limits the performance of solar cells fabricated with this material. The most striking feature of CIGS is the tolerance of the compositional variations in the chalcopyrite phase, such as Cu composition (22%-24%) in CIS. The mechanism of compositional variation in chalcogenic CIS will be discussed in Section 2-3.

## ***2-3. Phase Diagram***

Due to the multitude of elements and compounds were involved in the formation of CIGS defects, the phase diagrams have been extensively investigated by Gödeck [16]. These investigations had a special focus on the temperature and composition relevant for the preparation of thin films. Fig.

2-2 displays a simplified version of the ternary phase diagram, which comprises all ternary Cu-In-Se compounds. This ternary phase diagram, can be reduced to a simpler pseudo-binary phase diagram along the tie line between  $\text{Cu}_2\text{Se}$  and  $\text{In}_2\text{Se}_3$  (dotted line in Fig. 2-2) [38]. The bold points along this line represent the range of photovoltaic-quality material. By combining these two compounds, CIS chalcopyrite phase can be formed:

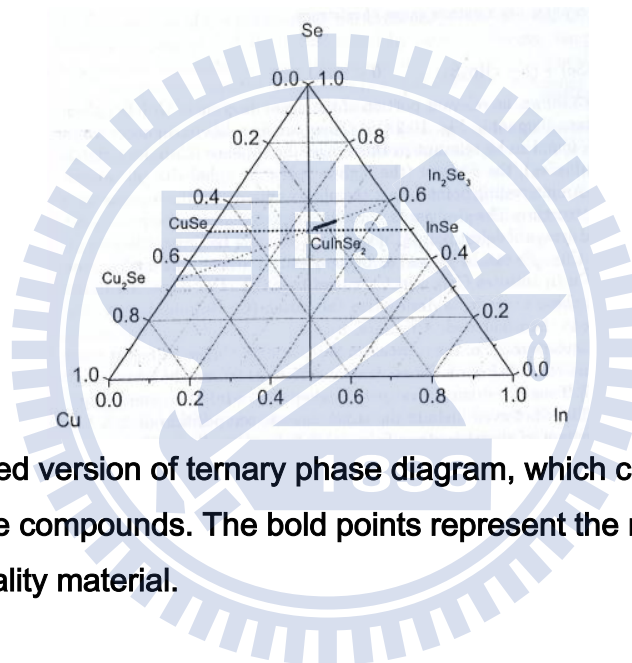
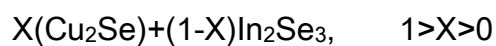


**Fig. 2-2 Simplified version of ternary phase diagram, which comprises all ternary Cu-In-Se compounds. The bold points represent the range of photovoltaic-quality material.**

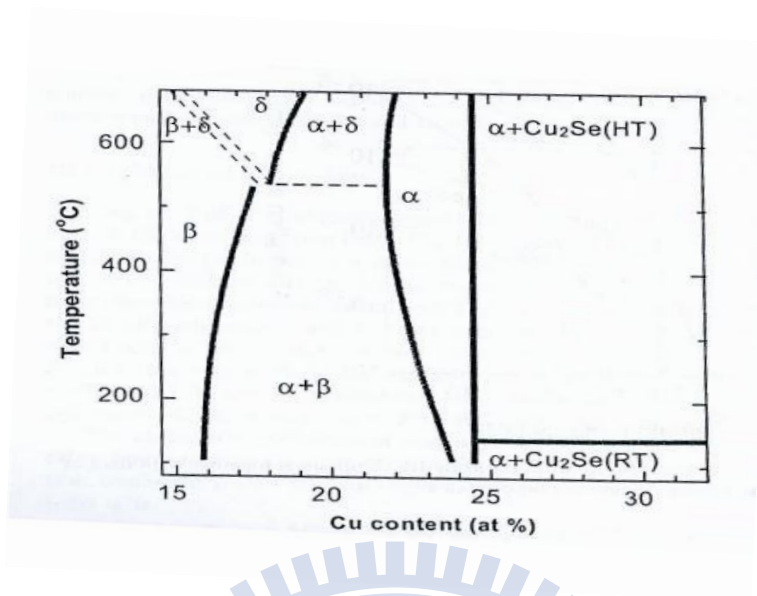
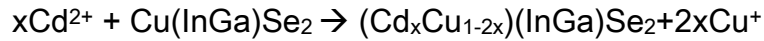


Fig. 2-3 Pseudobinary snapshot Cu<sub>2</sub>Se-In<sub>2</sub>Se<sub>3</sub> of ternary phase diagram in Fig. 2-2. The  $\alpha$ -phase has narrow range of existence.

Fig. 2-3 shows the relevant part of the CIS phase diagram [38]. There are four different phases which have been found to be relevant in this range: the  $\alpha$ -phase (CIS),  $\beta$ -phase (CuIn<sub>3</sub>Se<sub>5</sub>),  $\delta$ -phase (high temperature sphalerite phase), and Cu<sub>2-y</sub>Se. An interesting point is that the phases adjacent to the  $\alpha$ -phase have a similar structure. The  $\beta$ -phase is actually a defect chalcopyrite phase built by ordered arrays of defect pairs (Cu vacancies  $V_{Cu}$  and In-Cu antisites  $In_{Cu}$ ). The  $\beta$ -phase also can help the Cd<sup>2+</sup> diffusion to CIGS film. Wada et al. reported that when CIGS films were soaked in the Cd<sup>2+</sup> aqueous solution, Cd atoms were doped in the CIGS surface by the substitution of Cu atoms in the CIGS film by Cd ions in the solution [14]. Cd atoms are doped in the CIGS surface by substitution reaction such as,



Cd was reported to be more easily doped in the  $CuIn_3Se_5$  than in the  $CuInSe_2$ .  $Cu_{2-y}Se$  can be viewed as being constructed from the chalcopyrite by using Cu-In antisites  $Cu_{In}$  and Cu interstitials Cu [14]. The liquid phase  $Cu_{2-y}Se_{(l)}$  helps the grain growth of the CIGS chalcopyrite, as shows in Fig. 2-4 [15]. The existence range of the  $\alpha$ -phase in pure  $CuInSe_2$   $Cu_2Se$  -  $In_2Se_3$  (Fig. 2-3) at room temperature extends from a Cu content of 24% to 24.5% on the quasi-binary tie line [14]. Thus the range of the single  $\alpha$ -phase CIS is astonishingly small and does not even include the stoichiometric composition of 25% Cu. At the growth temperature of  $500^\circ C \sim 550^\circ C$ , the range of single CIS phase is expanded from 22% to 24%. Hence, the phase in deposition CIGS absorber is really complex. Fortunately, it turns out that partial replacement of In with Ga, as well as the use of Na containing substrates, considerably widens the single phase region in terms of  $(In+Ga)/(In+Ga+Cu)$  ratios [17]. Thus, the connection with addition of Ga and Na explains the substantial improvements actually in recent years either by adding Na to the growth process or from Na containing substrate (SLG).

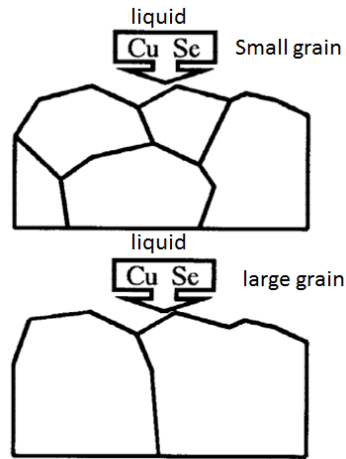


Fig. 2-4 crystal growth and change of the phases in the CIGS films during liquid  $\text{Cu}_{2-y}\text{Se}$  phase.

## 2-4. Defects and Impurities

The role of defects in the CIS ternary compound, and even more so in CIGS, is of special importance because of the large number of possible intrinsic defects and the role of deep recombination centers in the performance of the solar cells. The challenge of defect physics in CIGS is to explain three unusual effects in this material [18-19]:

- Doping of  $\text{Cu}(\text{In},\text{Ga})\text{Se}_2$  with native defects.
- The electrical tolerance to large off-stoichiometries.
- The electrically neutral of the structural defects.

It is obvious that the explanation of these effects significantly contributes to the explanation of the photovoltaic performance of this material. It is known that the doping of  $\text{CuInSe}_2$  is controlled by intrinsic defects. Samples with p-type conductivity are grown if the material is Cu-poor and annealed under high Se vapor pressure, whereas Cu-rich materials with Se deficiency tends to be

n-type [19-20]. Thus, the Se vacancy ( $V_{Se}$ ) is considered to be the dominant donor in n-type materials (and also the compensating donor in p-type materials), and the Cu vacancy ( $V_{Cu}$ ) is the dominant acceptor in Cu-poor p-type materials.

In contrast to the binary compounds, where small deviations from stoichiometry cause drastic changes of the electronic properties, the ternary compounds, in particular CIS phase, are much more tolerant. The Cu content of device-quality of CIS or CIGS absorbers varies typically between 22 and 24 at% Cu. Thus, these films are markedly Cu-poor but nevertheless maintain excellent semiconducting properties. In terms of point defects, a non-stoichiometry of 1% corresponds to a defect concentration of roughly  $10^{21}$   $cm^{-3}$ , by about five orders of magnitude more than the acceptable density of recombination centers in a photovoltaic absorber material and on the order of the net doping concentration of about  $10^{17}$   $cm^{-3}$  that is useful for the photovoltaic active part of a solar cell. Even if we allow a degree of compensation of 99%, the respective densities of donors and acceptors would be only in  $10^{19}$   $cm^{-3}$  range. The virtual number of defects calculated from off-stoichiometry has to be brought down to reasonable quantities that are compatible with the good electronic quality required for a photovoltaic. The incorporation of Ga and Na inhibits the ordering of the defect complexes and hence the formation of secondary phases in the bulk of the thin film [21]. The surface of the In-rich film exhibits the 1-3-5 composition of the  $Cu(In,Ga)_3Se_5$

defect phase [22]. In the other word, the surface is always more Cu-poor than the bulk of the material, which can enhance the  $\text{Cd}^{2+}$  diffusion to the CIGS film. The precise properties of this surface defect layer are not yet known. However, it is of high importance that the band gap at the surface of the  $\text{Cu}(\text{In,Ga})\text{Se}_2$  thin films is somewhat larger than the band gap in the bulk of the material [22].

On the Cu-rich side of the single-phase region of the phase diagram,  $\text{Cu}_2\text{Se}$  segregates as a secondary phase. In thin films,  $\text{Cu}_2\text{Se}$  can be easily removed by dissolving in potassium cyanide (KCN) solution leaving behind a CIS or CIGS film with the proper stoichiometry. The  $\text{Cu}_2\text{Se}$  phase is a binary phase that exhibits good conductivity. However, the solar cell made from the absorber grown in the Cu-rich method is far less efficient than those with slightly Cu-poor absorber.

## ***2-5. Band gap of various compounds***

The present design of a standard cell is the result of an historic development- based upon empirical optimization. Improved knowledge about the materials and devices now allow systematic developments. The exploitation of the chalcogenic material system expanded considerably in the recent past. Alloys of multinary chalcopyrite compounds allow all kinds of band gap variations in the absorber film. Fig. 2-5 presents an overview of the possibility of band gap engineering and the design of wide band gap devices

in the  $\text{Cu}(\text{In,Ga,Al})(\text{S,Se})_2$  system. The band gap of this chalcogenic system displayed in Fig. 2-5 covers the visible spectrum with a wide range from 1.04 eV in the CIS to 2.7 eV in the  $\text{CuAlSe}_2$  (CAS) phase. Fig. 2-5 summarizes lattice constants and band gap of this system. Any desired alloys between these compounds can be produced, as there is no miscibility gap in the entire system.

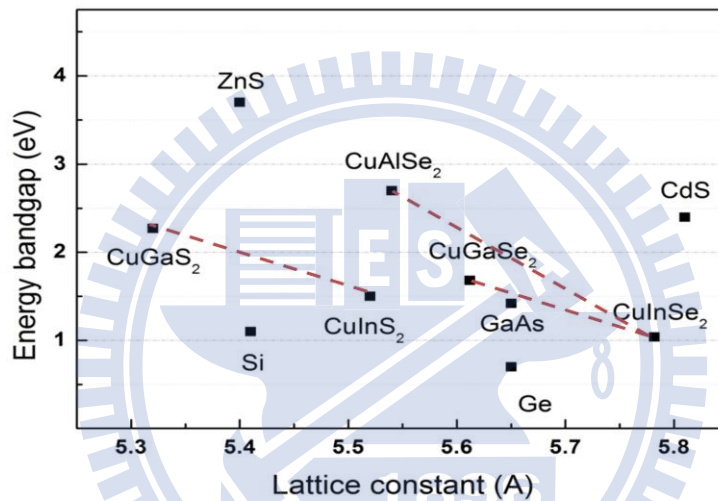


Fig. 2-5 Energy band gap of various semiconductor.

## 2-6. High-Efficiency Techniques

One of the important parameters to obtain high efficiency in CIGS-based solar cells is the  $\text{Cu}/\text{III}(\text{In}+\text{Ga})$  ratio in the film. As shown in Fig. 2-6, high efficiencies of over 10% are obtained in a relatively wide range of  $\text{Cu}/\text{III}$  ratios from 0.75 to 0.95. The CIGS device made by the absorber with the  $\text{Cu}/\text{III}$  composition higher than 0.95 shows poor photovoltaic quality due to undesired Cu-related secondary phases with significantly low resistivity



On the other hand, the Ga/(In+Ga) ratio of bulk CIGS film is typically between 0.2 and 0.3. The increasing of the Ga/(In+Ga) ratio (larger than 0.4) degrades the cell efficiency. For the CIGS absorber fabricated by three-stage evaporation, the film property of graded band gap is shown in Fig. 2-7. The graded band structure improves the effective hole diffusion length within the absorber region, and mitigates the internal recombination of holes and electrons. The open-circuit voltage of CIGS thin film solar cells is roughly expressed by the following equation:

$$V_{oc} = \frac{E_g}{e} - 0.5 \text{ (V)}$$

For a Ga composition ratio smaller than 0.3, where  $E_g$  is the band gap for CIGS. However, the open-circuit voltage for Ga compositions above 0.4 becomes lower than expected. The reason for this is partly the degradation of film quality (small grain size) and type conversion of the surface layer from n-type to p-type. In the conventional CIGS cells, the surface layer is n-type because of the diffusion of Cd during the CBD process of CdS deposition and also the formation of n-type  $\text{Cu}(\text{InGa})_3\text{Se}_5$  (OVC, ordered vacancy phases).

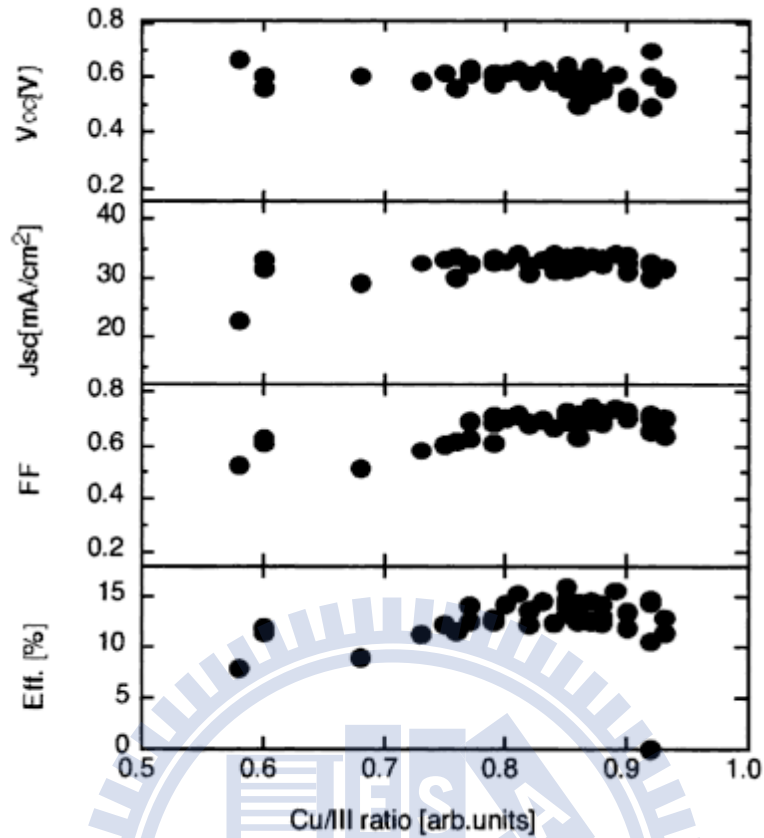


Fig. 2-6 Photovoltaic performances of CIGS thin-film solar cells as a function of Cu/III ratio.

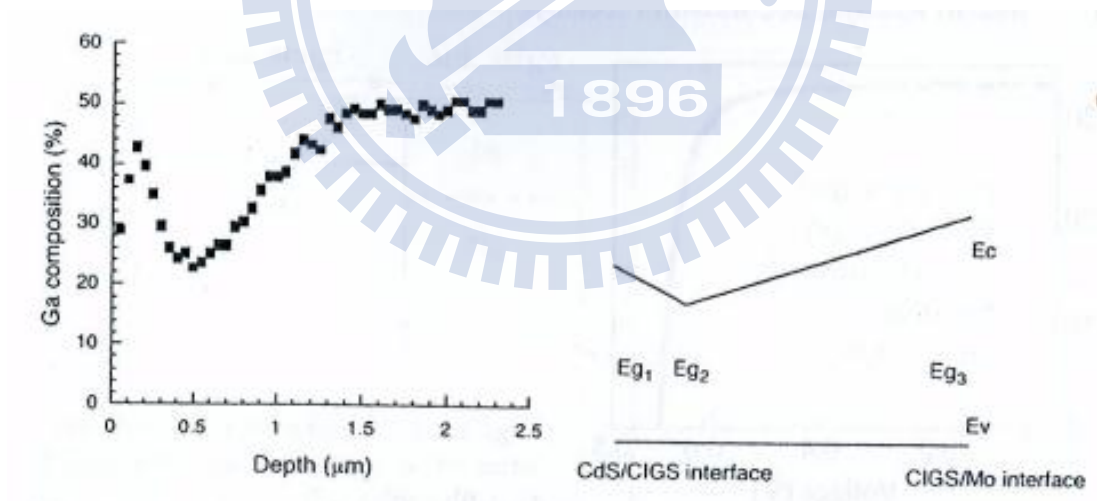


Fig. 2-7 Bandgap profiling of CIGS solar cell: (left) Auger analysis of Ga composition, (right) graded-bandgap structure.

There is a V-shape band gap structure shown in right figure of Fig. 2-7. The band gap  $E_{g1}$  is slightly smaller than  $E_{g2}$  and  $E_{g3}$ . The increasing from  $E_{g2}$  to

$E_{g3}$  is helpful to higher open voltage. On the other hand, the slightly higher band gap  $E_{g1}$  than  $E_{g2}$  will result in back side field (BSF) effect, which improves the carrier collection. Therefore, it can be concluded that to form V-shape band structure by controlling the Ga distribution is a critical factor to achieve high conversion efficiency [38].

## ***2-7. CIGS absorber layer fabrication***

Chalcopyrite CIGS films can be fabricated by both vacuum and non-vacuum processes. However, the cell efficiency with the absorber formed by vacuum processes generally reveals high efficiency than that of non-vacuum one. In this study, vacuum processes of the co-evaporation method and the selenization process of precursors will be introduced in following sections.

### **Co-evaporation**

Co-evaporation is the best method among the CIGS deposition techniques especially for laboratory scale devices because of its flexibility in evaporation process. The cells efficiency over 20% has been achieved by using co-evaporation method by the Zentrum für Sonnenenergie-und Wasserstoff-Forschung (ZSW, Center for Solar Energy and Hydrogen Research) Baden-Württemberg, Germany [23]. The typical co-evaporation facility for fabricating CIGS thin films is shown in Fig. 2-8. The vacuum co-evaporation chamber consists of four evaporation sources, a sample holder, and a heater.

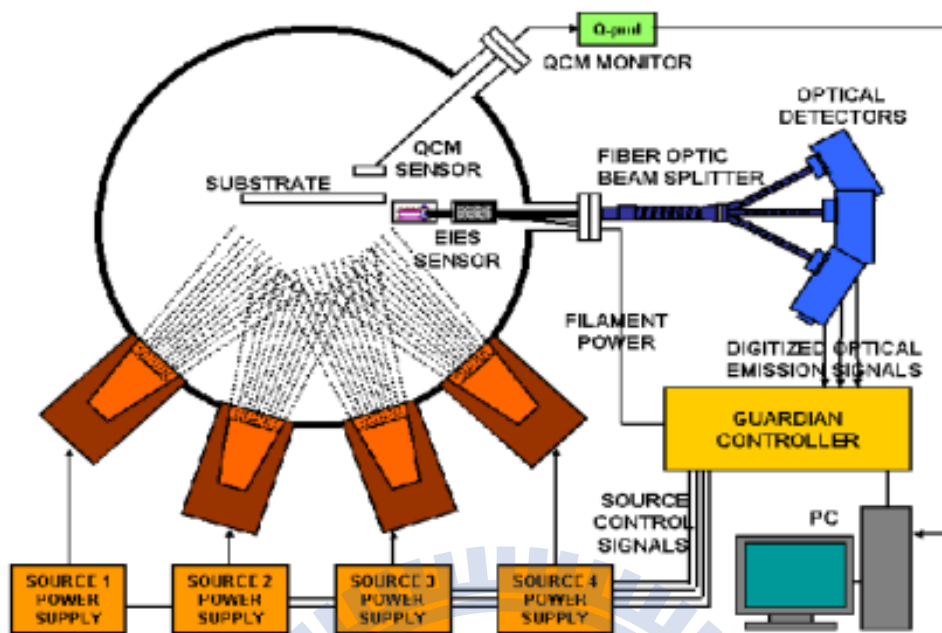


Fig. 2-8 Schematic of co-evaporation method.

The most successful modification of the inverted process is the so-called *three-stage process*, as shown in Fig. 2-9 [24]. In this process, In, Ga, and Se are again evaporated at the end of an inverted process again to ensure the overall In-rich composition of the film, even if the material is Cu-rich during the second stage. The absorber formed by the three-stage process has shown best film-qualities with respect to cell efficiencies. In general, variations of the Ga/In ratio during deposition, allows the design of graded band gap structures to be accomplished (V-sharp) [21-22]. The nucleation phase of the films is important and should have controlled conditions so as not to create large, isolated grains and to obtain smooth, dense films in the three-stage process. Co-evaporation can be realized easily only for relatively small areas. It is difficult to control the four element deposition on larger-area substrates.

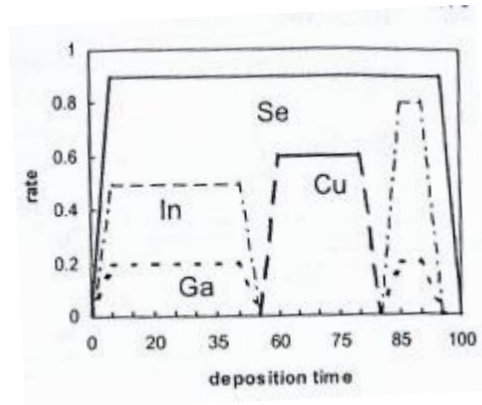


Fig. 2-9 three-stage process.

## Selenization

The complexity of the equipment for co-evaporation processes can be circumvented if the layer can be formed from elemental or compound precursor films. These precursor films can be prepared by lots of methods for thin-film deposition. Fig. 2-10 illustrates the different possibilities for film formation by reactive processes. The second class of absorber preparation routes is based on the separation of deposition and compound formation into two different processing steps. Efficiency of over 10% is achieved by using the absorbers prepared by selenization of metal precursors in  $H_2Se$  or by rapid thermal processing (RTP) of stacked precursor film in the Se atmosphere [27-29].

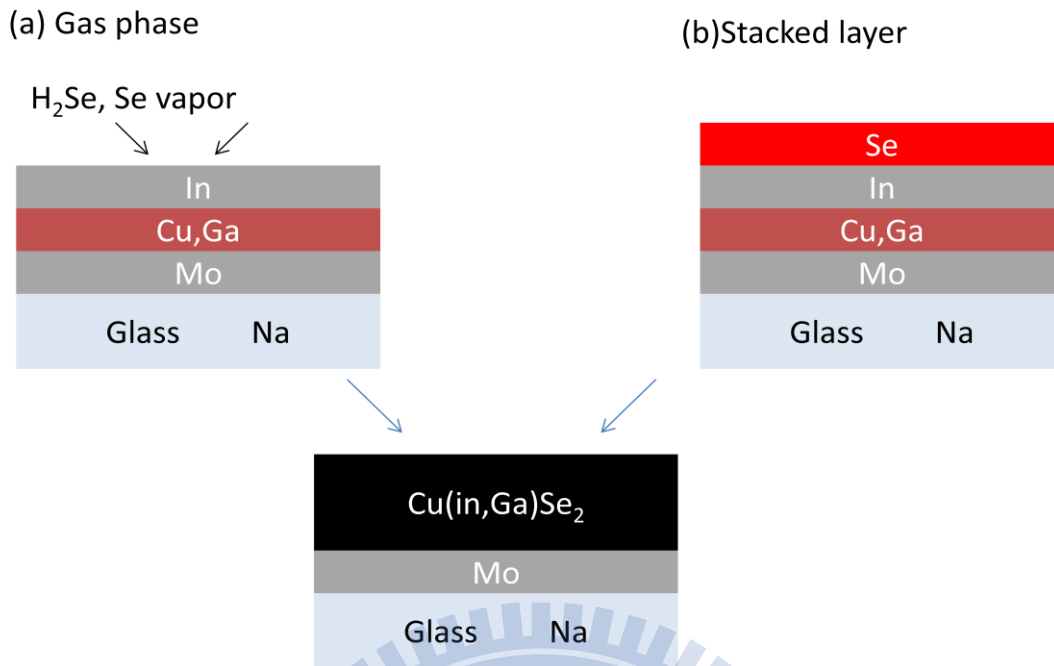


Fig. 2-10 illustration of selenization process a) with Se/H<sub>2</sub>Se vapor, and b) Se is provided by a solid layer.

## 2-8. Motivations

The detailed and sophisticated controls over compose and growth achievements during co-evaporation are hard to construct for the selenization process. The reaction kinetics is controlled by the heating duration and temperature of the annealing process. Therefore, the poor-adhered and degraded selenization qualities are the issues of the selenization process. On the other hand, the formation of CuInSe<sub>2</sub> is much faster than that of CuGaSe<sub>2</sub>. Because the formation of the ternary chalcopyrite phase starts at the initial reaction at the front surface, Ga tends to diffuse and accumulate to the back surface of the film (CIGS and Mo interface). The larger Ga/III(In+Ga) ratio implies the larger band gap, which benefits the open circuit voltage (V<sub>oc</sub>) of

device efficiency. Moreover, graded Ga distribution (V-shape) introduces the BSF effect, which improves the carrier collection as well as the reduction of back-surface recombination. However, the bottom accumulated Ga results in low  $V_{oc}$ , and subsequently induces the secondary phase  $Cu_{2-x}Se$  at the surface region.

In this research, we not only studied the formation procedure of CIGS film, but also discussed the temperature-relevance of selenization during grain-crystallization to improve the absorber film. Firstly, the growth mechanism of  $CuInSe_2$  thin films by sputtering and selenization process in stacked layer Se instead of toxic gas  $H_2Se$  was discussed. The three growing paths of CIS films determined by analyzing  $Cu_{2-x}Se$  and  $\beta-In_2Se_3$  binary compounds layers using two-step process are reported. Subsequently, CIS films were prepared with each growing path. Crystallization, morphology, and phase determination on selenized CIS films were examined, as well as the formation of  $Cu_{2-x}Se$  and  $\beta-In_2Se_3$  binary compounds at various annealing temperatures. Based on those results, the method to obtain CIS absorber by selenization was then optimized. Moreover, A four-step annealing process instead of conventional Ar treatment to mitigate the Ga accumulation issue, as well as to enhance the adhesion between CIGS and Mo films were also proposed in this thesis.

# Chapter 3

## Experimental

This chapter will cover the NCTU deposition system, including a sputter chamber and a selenization chamber, for fabricating the CIGS absorber film. Analyzing tools such as scanning electron microscope (SEM), energy dispersive spectrometer (EDS), X-ray diffraction (XRD), and Raman spectrometer will be included as well.

### *3-1. CIGS deposition system*

To deposit CIGS thin film, a self-designed CIGS deposition system was used in this thesis. This deposition system consists of a sputter and a selenization chamber. A vacuum load-lock connects the sputter and the selenization chamber so that the sample can be maintained in a relatively clean environment during the fabrication process.

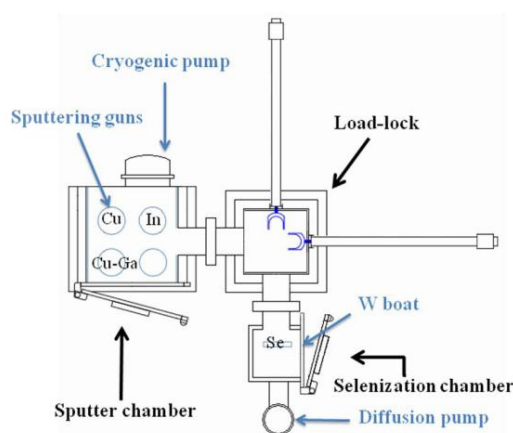


Fig. 3-1 Schematic of NCTU deposition system.



## Sputter system

To deposit the metallic precursors such as Cu, In, Cu-Ga, as well as the back contact metal, Mo, sputter is a primary facility. To understand the sputter system, the principle is introduced.

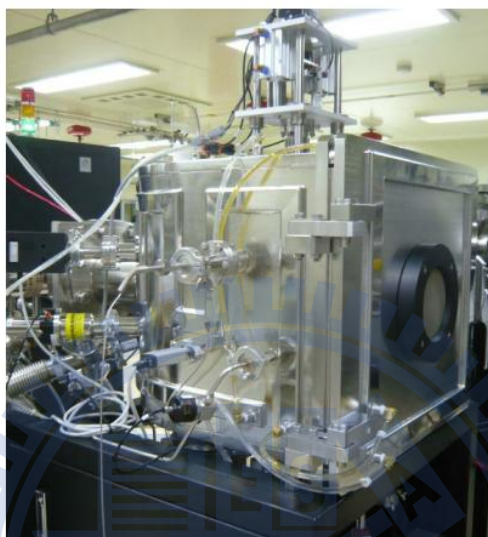


Fig. 3-2 NCTU sputter system.

## Principle of NCTU sputter system

Sputter is a process by which energetic ions or neutral atoms strike the surface of a solid material causing ejection of atoms or molecules by momentum transfer.

In a typical sputtering process, after the chamber is evacuated, the working gas, Ar, is introduced into the chamber until the pressure in the chamber rises to the mTorr region. The target is then biased to a direct current (DC) or radio frequency (RF) negative electric potential, and plasma is struck between the negatively biased target and the substrate holder. The mobile particles in the plasma sustain the glow discharge. For the positively charged particles, they

are driven by the potential gradient across the chamber and accelerated to strike the surface of the target and dislodge atoms or molecules. The ejected atoms or molecules then travel through the chamber and finally deposit onto the substrate. A schematic of the sputter process is shown in Fig. 3-3. The NCTU sputter system consists of a power supply, a chamber, ground shields, working gas, vacuum pumps, targets, and a sample holder.

To generate the plasma, a power supply is required. The generation of plasma can be done by applied either DC or RF. Power supply is used to apply a negative bias to the substrate in order to increase ion bombardment of the film during deposition. A chamber is used to maintain the working environment at a preferred vacuum level. The ground shield is conformal and is placed as close as possible to the target body. The working gas in the sputtering process generally has three criteria. First, the gas should be inert to the material being deposited; second, it should have the ability to provide a high sputtering yield; third, for practical applications, it should be relatively inexpensive and readily available in high purity. Among the gases, Ar is easy to generate the plasma by ionization; it also meets these requirements and is chosen to be used in this thesis.

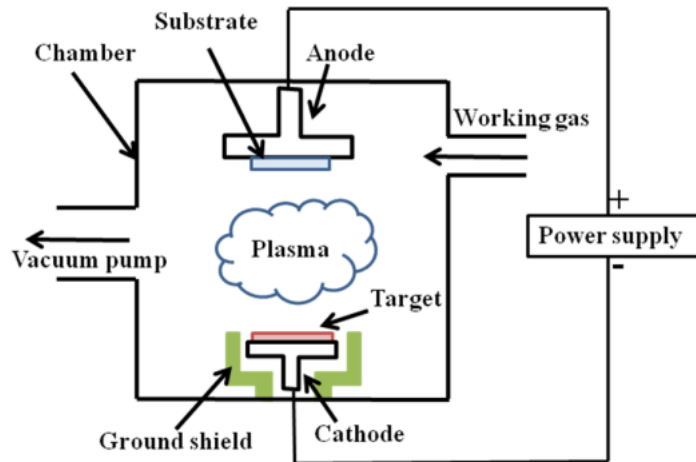


**Fig. 3-3 Schematic of sputter.**

To achieve the desired vacuum level, a mechanical pump and a cryogenic pump are used. The mechanical pump is an oil-sealed rotary pump, which is used to establish the necessary fore vacuum for the cryogenic pump. It can bring the chamber pressure from atmosphere to around 50 mTorr. Cryogenic pump is based on the principle of cold trap. Over periods of removal and entrapment, by freezing the molecules onto the cooled surface of the high surface area array, the pressure in the chamber becomes lower.

Target is the material to be deposited onto the substrate. It usually has a smooth surface and symmetrical shape. In this thesis, Cu, In, Mo, and Cu-Ga alloy targets are used. The purpose of sample holder is easily to be understood. Although the sample holder may not seem to be an important feature of sputter, in practice, it serves to not only hold the substrate in place but also to act as an electrode, a temperature controllable assembly and as the interface with the substrate handling system.

## Selenization system

The selenization system is utilized to selenize the metallic precursors deposited by the sputter system mentioned above. Selenization combines evaporation of Se and annealing process, which are essential in the formation of desired CIGS films.

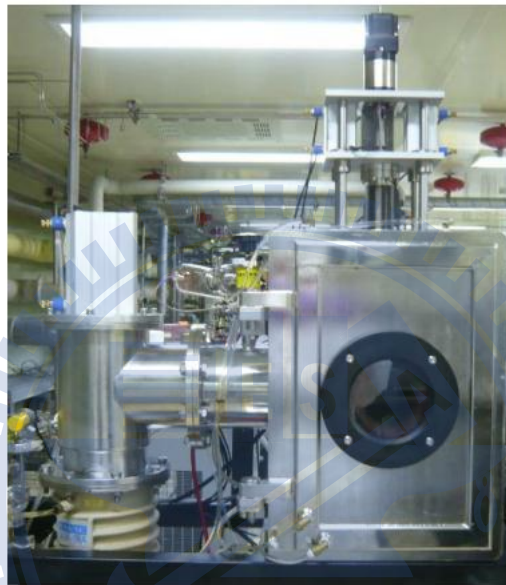


Fig. 3-4 NCTU selenization system.

## Principle of NCTU evaporation system

Evaporation is a deposition method involving the heating of a source material to sufficiently high temperature under vacuum so that atoms or molecules are liberated from the source, travel through the vacuum and deposit onto a substrate. This method includes three parts: 1) the transition of desired material from condensed phase to vapor phase, by heating the source material, 2) transportation of vapor from source to substrate, and 3) condensation and film growth on a sample surface. A schematic of NCTU

evaporation system is shown in Fig. 3-5. The evaporation system consists of a stainless steel chamber, vacuum pumps, an evaporation source, a halogen lamp, and a substrate holder.

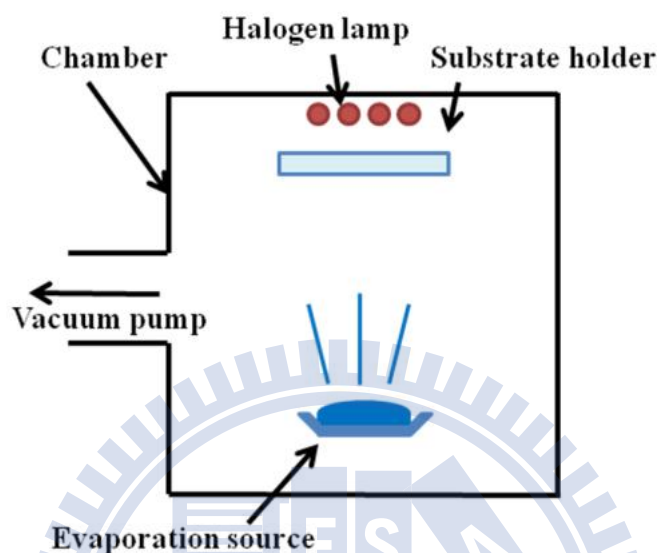


Fig. 3-5 Schematic of evaporation.

The chamber is box-like in shape. The main purpose of chamber is to maintain the high vacuum level needed for the evaporation process. High vacuum ( $10^{-5}$ –  $10^{-8}$ Torr) in the chamber is required for reducing the residual gas impurity levels, minimizing the molecule absorption rate onto the substrate surface as well as decrease the amount of unnecessary gas phase collisions.

To attain the vacuum level, two pumps are used in our experiment: a mechanical pump and a diffusion pump. Except for launching the requisite fore vacuum for the later high vacuum pump, i.e. diffusion pump, rotary pump also serves to assist the diffusion pump by constantly removing gas collected by diffusion pump. Diffusion pumps use low vapor pressure oil heated to around  $200^{\circ}\text{C}$  which percolated at high velocity through a series of baffle plates to

remove gas molecules from the chamber by a collision mechanism and achieve high vacuum level. (A point is worth mentioned that the back streaming of oil from the heated diffusion pump into the processing chamber may occur, which may contaminate the sample.) Selenium is placed in a thermally heated tungsten boat (W boat) to vaporize, where Se is the evaporated source, W boat is the container. Thermodynamically the partial pressure of the source material in the gas phase have to be greater than the partial pressure of source material in the condensed phase in order to have condensation and film growth to occur at the substrate.

### **Annealing process**

After the evaporation of elemental Se on the precursor film, an annealing process in the Se-containing environment is applied. This annealing process, which is also called selenization process when fabricating CIGS, is a heat treatment that involves heating and maintaining the specimen to a selected temperature for a period, and then cooling. Through the selenization process, removal of defects in crystal and re-crystallization of Cu-In-Ga alloy with elemental Se would occur. The chemical properties as well as physical properties of precursors might change after selenization process.

## ***3-2. Analytical technologies***

In this section, four analytical tools will be presented, including SEM, EDS, XRD, and Raman scatter.

### **Scanning electron microscopy (SEM)**

Scanning electron microscope (SEM) is the facility that allows us to examine the sample's topography. Unlike the conventional optical microscope using light, SEM utilizes electrons to reveal the image of the specimen. In SEM, electrons from thermionic or field-emission cathode are accelerated between a cathode and an anode. The electron beam is finely focused into a small-diameter electron probe and scanned simultaneously in two perpendicular directions over a sample surface, making use of the fact that electric or magnetic fields, applied at right angles to the beam, can be used to adjust its direction of travel. Since the pressure in the specimen chamber usually amounts to about  $10^{-4}$  Pa, the electron beam is allowed to travel from the cathode to the specimen with little interaction with the residual gas molecules. When the accelerated high-energy electron beam bombards the sample, the interaction of the beam with the sample material generates a variety of responses, including secondary electrons emission, back scattered

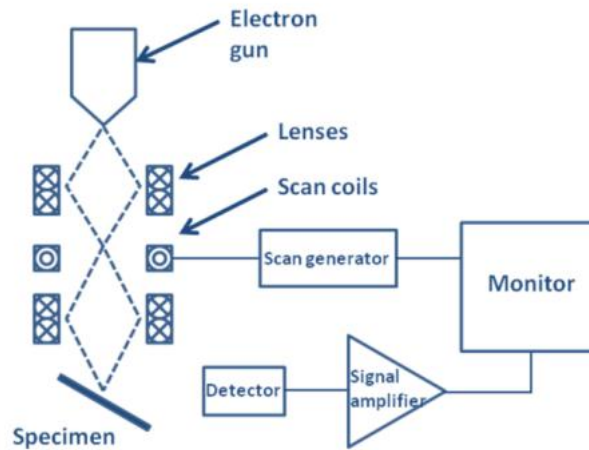


**Fig. 3-6 Schematic of SEM.**

electrons emission, x-ray emission, and Auger electrons emission. By collecting the resulted responses and signals, the image is formed on a monitor after first converting information from the specimen surface into a train of electrical signals. Therefore, the image formation in the SEM differs from that of the conventional light microscope. The SEM is often the primary facility used to provide a magnified image of an area of the sample to be examined especially on a micro-scale.



**Fig. 3-7 SEM at NCTU.**



## **Energy dispersive X-ray spectroscopy (EDS)**

Energy dispersive spectroscopy (EDS) is capable of identifying heavy elements in a few minutes. It is a rapid technique for atomic identification in the material of interest. This technique is a specific technique for the detection and energy distribution determination of the characteristic X-ray. The emission of the characteristic X-ray is a phenomenon produced by inner-shell excitation with incident electrons. Because the characteristic X-ray has specific energy corresponding to each element, the element can be identified from the peak energy. The identification of element from the emission of the characteristic X-ray is as followed. After the generated characteristic X-ray passes through a thin window into a solid state detector, the detector converts the incoming X-ray photons into electron-hole pairs, which are driven out of the detector and further converted to an electronic pulse by a charge-sensitive preamplifier. The amplitude of the pulse is directly proportional to the energy of the detected X-ray. A signal corresponding to the energy is processed into the appropriate channel of a multi-channel analyzer. The signal processing electronics calculates the number of pulses, resulting in a histogram of X-ray energy versus intensity. Furthermore, because of X-ray absorption in the beryllium detector window and in the lithium-drifted silicon chip itself, elements with atomic number less than ten are not usually identified.

## X-ray diffraction (XRD)

X-ray diffraction (XRD) is mainly for identifying the crystalline phases and determining the orientation as well as the grain size. In XRD, a collimated beam of monochromatic X rays strikes a specimen and is diffracted by crystal planes. By Bragg's law,

$$\lambda = 2d\sin\theta$$

we can calculate the spacing between planes,  $d$ , from the wavelength of incident X-ray,  $\lambda$ , and the diffraction angle,  $2\theta$ , which is scanned to pick up diffraction from the different crystal planes. By measuring the X-ray profile and further calculation, the orientation of planes of the specimen can be obtained.

A schematic of XRD is shown in Fig. 3-8. XRD consists of an X-ray tube, a detector, and slits. X-rays generated from an X-ray tube are divergent; they travel towards the sample through the slits that can define the incident X-ray beam by limiting the divergence of the X-ray beam and can further influence the peak intensity as well as the peak shapes. Since CIGS is a crystalline semiconductor, it is characterized by the orderly periodic arrangements of atoms. These atoms can be seen as a periodic array and thus can diffract light. A detector is used to detect the diffraction X-ray profile. By using the position and relative intensity of a series of peaks to match experimental data to the reference patterns in the database, we can derive the orientations in CIGS. In polycrystalline CIGS thin film, some planes are found to be more oriented in a particular direction than in the others. This presence state is common to all

polycrystalline thin films and when this type of orientation is prominent, the crystalline substance is then said to have preferred orientation. In this thesis, in order to increase the cross section of the sample to be detected, the incident angle of the X-ray was set to be at a small angle ( $<3^\circ$ ). Therefore, a large area of the sample surface was detected and the preferred orientation was obtained.

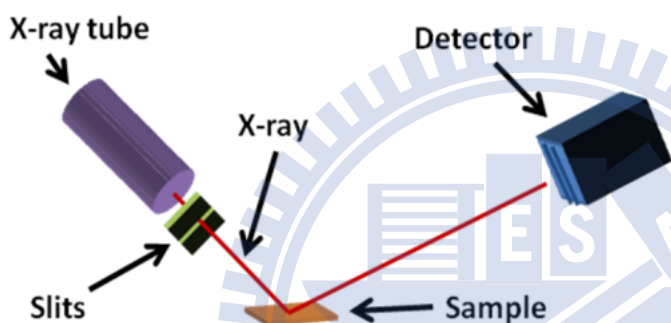


Fig. 3-8 Schematic of XRD.



Fig. 3-9 XRD at National Device Laboratory.

## Raman scattering

Raman scattering (RS) has been established among optical methods as a fast, sensitive, and nondestructive method to investigate the material information, including the crystalline quality and homogeneity of materials as well as their electronic properties. Raman scattering is a function of the lattice vibration interaction. Since lattice vibrations are very sensitive to local environments, Raman scattering can give information about material structure

and quality on the scale of a few lattice constants. Raman scattering can characterize the semiconductor materials, either in bulk, thin film, or device form. For the II-VI semiconductor materials as well as their ternary and quaternary alloys, these materials are usually identified by the frequencies of their zone center optical modes. With the knowledge of the composition dependence of the phonon frequency and excluding other effects, which can also shift the mode frequency, the composition of alloys can be obtained with high accuracy. In this thesis, Raman scattering is required to evaluate the thin film quality and to distinguish between the CIGS and  $\text{Cu}_{2-x}\text{Se}$  phases that are not easy to be separated by XRD.

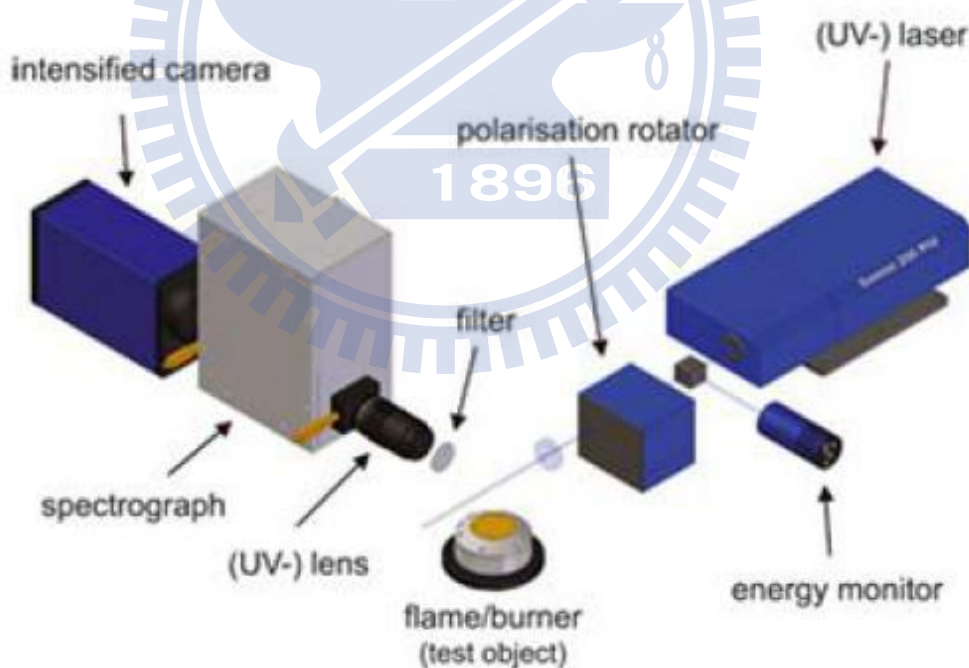


Fig. 3-10 Schematic of RS



Fig. 3-11 Raman at Nano Facility Center (NFC), NCTU.



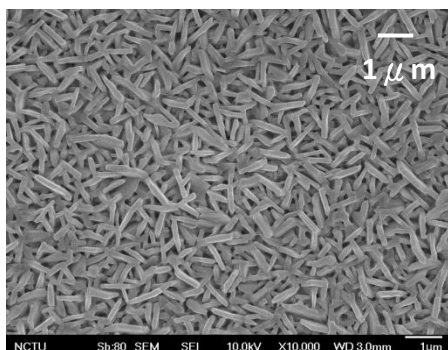
# Chapter 4

## Results and discussion

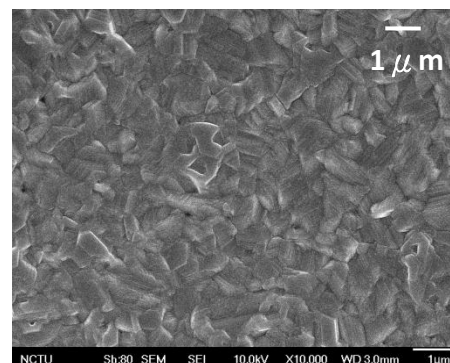
### *4-1. Cu-Se phase*

Prior to fabricating CIS and CIGS absorbers, the formation condition of major binaries ( $\text{Cu}_{2-x}\text{Se}$  and  $\text{In}_2\text{Se}_3$ ) should be identified first. We started from depositing Copper and selenium on SLG substrates, and annealed the SLG/Cu/Se samples at various temperatures for 30min. The percentages corresponded to fractions of the total thicknesses of Cu and Se layers of 0.2  $\mu\text{m}$  and 0.8  $\mu\text{m}$ , respectively. Fig. 4-1 shows the plane-view SEM micrographs of Cu-Se binaries at annealing temperatures of 150°C, 250°C, 350°C, 450°C, and 550°C, respectively. In Fig. 4-1(a), the sample annealed at 150°C exhibited caterpillar-like and small grains in crystallization. When the temperature was increased to 250°C, the grains were growing to about 1 $\mu\text{m}$  based on visual estimation, as shown in Fig. 4-1(b). Besides, the crystallization became smooth and compact in surface morphology. Similarly, smooth and large-grained films were obtained at the temperatures over 250°C, shown in Figs. 4-1(c) to (e). EDS and XRD analyses were also carried out to identify the crystal phase. From the results shown in Table 4-1, the composition ratio of Cu and Se was 1 for the sample annealed at 150°C, and approximately fixed to 1.8 at the samples annealed at the temperatures over 250°C, respectively. We

assumed CuSe phase was formed at 150°C, and the same result was characterized by XRD analysis [30]. On the other hand, EDS and XRD analyses indicated that the CuSe phase was subsequently re-crystallized to Cu<sub>2-x</sub>Se, which shows the composition of Cu 64% and Se 36%. As shown in Fig. 4-2, the major orientation of Cu<sub>2-x</sub>Se was 111/220 at the sample of 250°C. The ratio of 111/220 to other peaks was slightly increasing when the annealing temperature was elevated to more than 250°C. Nevertheless, the peak of 220-orientation was then decreasing and lower than that of 111-orientation at the sample of 550°C. That was attributed to the crystalline energy of 220-orientation is higher than that of 111-orientation. When the temperature was increased to 550°C, the film tended to be stable and preferred 111-orientation. Therefore, the formation temperature of Cu<sub>2-x</sub>Se was predicted and assumed to about 250°C in our system.

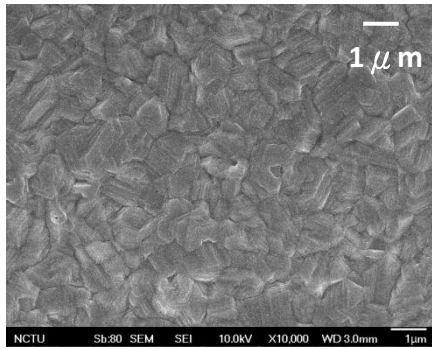


(a) 150°C

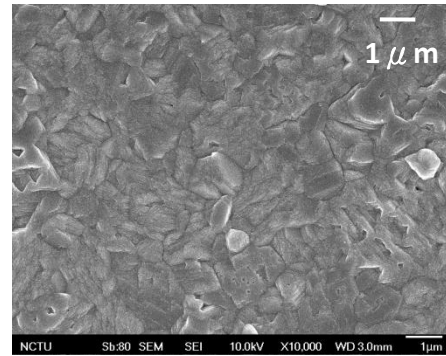


(b) 250°C

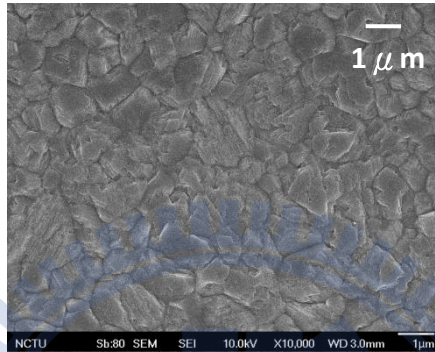




(c)350°C



(d)450°C



(e)550°C

Fig. 4-1 The SEM surface morphology of Cu-Se binary compound; (a) 150°C, (b) 250°C, (c) 350°C, (d) 450°C, and (e) 550°C.

Table 4-1 Cu-Se EDS analyses.

<i>Temperature</i>	<i>Cu(%)</i>	<i>Se(%)</i>
150°C	49.62	50.38
250°C	63.15	36.85
350°C	64.30	35.70
450°C	63.81	36.19
550°C	63.75	36.25



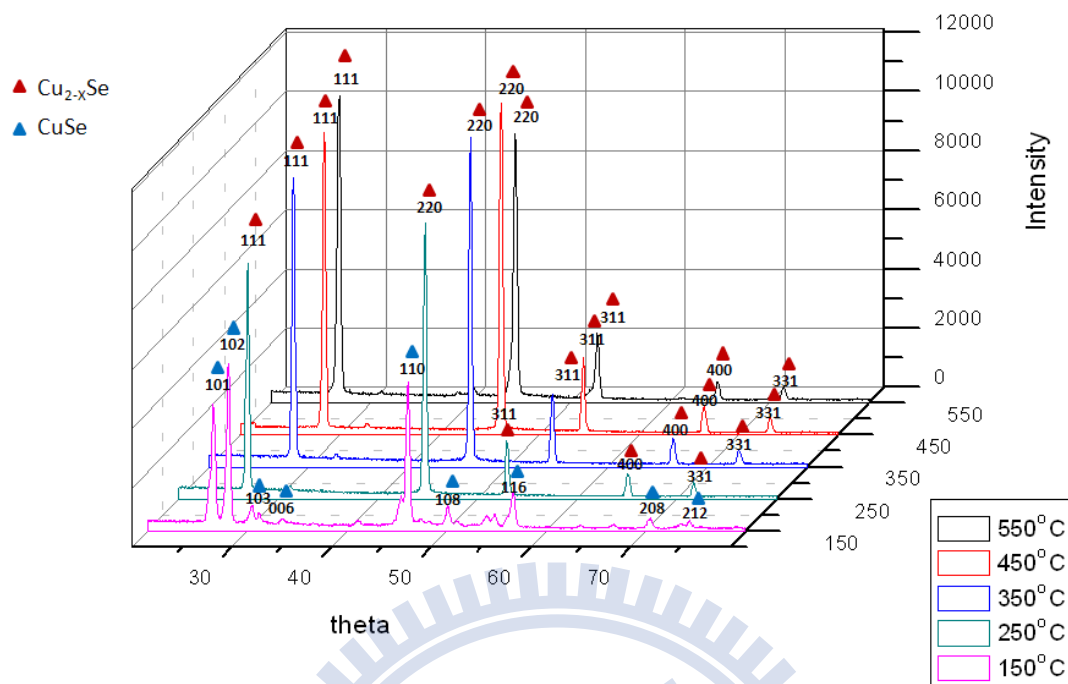


Fig. 4-2 Cu-Se XRD annealed in different temperature.

## 4-2. In-Se phase

For  $\text{In}_2\text{Se}_3$  phase, the formation temperature was examined by the selenization of indium precursor film. Indium and selenium were firstly deposited onto SLG substrates. The In thickness was  $0.3 \mu\text{m}$  and the Se was  $1.3 \mu\text{m}$ . After that, annealing process was carried out at the temperatures similar to that of Cu-Se samples. The duration of the annealing was fixed to 30min. Figs. 4-3(a) to (g) depict the SEM surface morphology of In-Se films with respective to the temperatures of room temperature (RT),  $150^\circ\text{C}$ ,  $250^\circ\text{C}$ ,  $300^\circ\text{C}$ ,  $350^\circ\text{C}$ ,  $450^\circ\text{C}$  and  $550^\circ\text{C}$ , respectively.

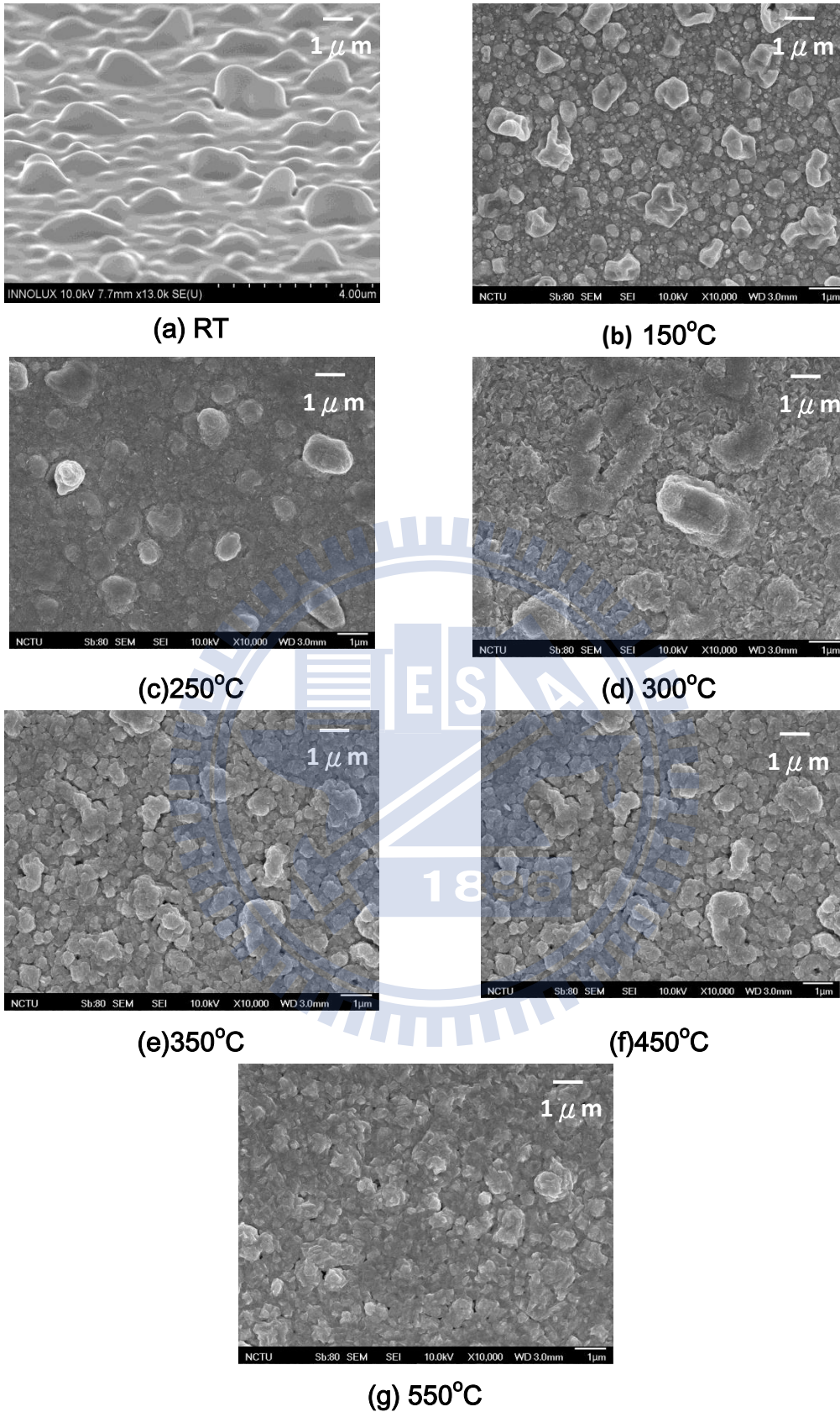


Fig. 4-3 The SEM surface morphology of In-Se binary compound annealed at (a) RT, (b) 150°C, (c) 250°C, (d) 300°C, (e) 350°C, (f) 450°C, and (g) 550°C.

From Fig. 4-3(a), a rough surface morphology is obviously observed at the sample of as-deposited In/Se film. The reason is that Indium shows high cohesion property like mercury. When indium is sputtered to the SLG substrate, it will be congregated together and form many non-uniform grains. It will result the sputtered Indium film to be rough surface and same situations in the subsequent selenium surface. Figs. 4-3(b) to (g) representing the In-Se films annealed at various temperatures reveal non-uniform grains in surface morphology. For the phase determination, EDS result reveals that the composition of In and Se was 31.48% and 68.52% at annealing temperature of 150°C, and became about 60% and 40% at elevated temperatures, respectively.

**Table 4-2 In-Se EDS analyses.**

<i>Temperature</i>	<i>In (%)</i>	<i>Se(%)</i>
150°C	31.48	68.52
250°C	59.64	40.36
300°C	59.27	40.73
350°C	58.89	41.11
450°C	59.50	40.50
550°C	59.52	40.48

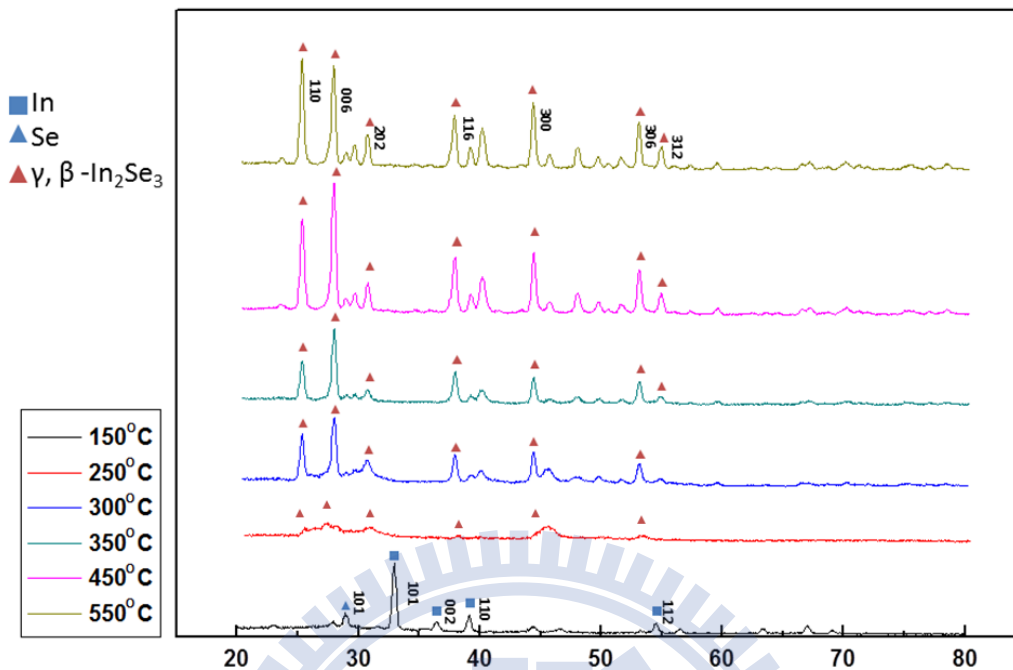


Fig. 4-4 In-Se XRD annealed in different temperature.

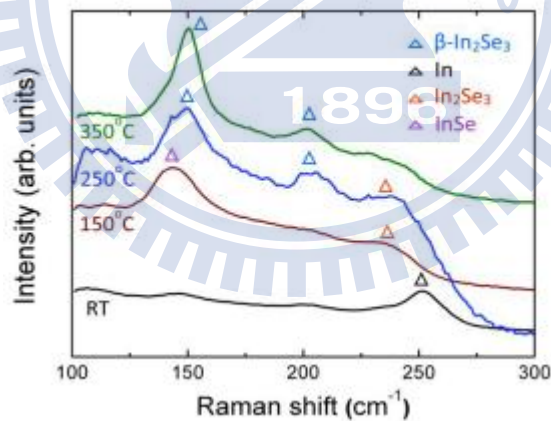


Fig. 4-5 In-Se raman annealed in different temperature.

Except to EDS characterization, XRD analysis and Raman shift were utilized to clarify the crystalline phase of the In-Se films [30]. Raman shift revealed that In-Se compounds start being reacted at 150°C and recrystallize to amorphous

$\text{In}_2\text{Se}_3$  ( $\alpha\text{-In}_2\text{Se}_3$ ) and beta-phase  $\text{In}_2\text{Se}_3$  ( $\beta\text{-In}_2\text{Se}_3$ ). The Raman shift at  $240\text{cm}^{-1}$  shows the presence of  $\alpha\text{-In}_2\text{Se}_3$ , as well as at  $150$  and  $205\text{cm}^{-1}$  is  $\beta\text{-In}_2\text{Se}_3$  phase, respectively [31]. From Figs. 4-4, 4-5, and Table 4-2, the results of  $150^\circ\text{C}$  sample reveal that a part of In and Se was reacted, and some remain elementary phase. However, non-reacted Se would be evaporated in the annealing procedure. It might be the reason that one-step annealing process is hard to achieve high selenization quality. This result is in good agreement with XRD analyses. When the annealing temperature was lower than  $250^\circ\text{C}$ , the XRD peak of  $150^\circ\text{C}$  sample represented In and Se elements in the film without reacting to In-Se compounds. On the other hand, small intensity in XRD peaks of  $250^\circ\text{C}$  annealing temperature were possibly attributed to amorphous In-Se compounds, which was the same observation in Raman results. While the annealing temperature was over  $350^\circ\text{C}$ , polycrystalline  $\beta\text{-In}_2\text{Se}_3$  phase was obtained in both Raman and XRD analyses. In Fig. 4-4, the intensity of the peak 006 started decreasing at  $450^\circ\text{C}$  sample, and was lower than that of peak 110 at  $550^\circ\text{C}$  sample. This situation is similar to Cu-Se results we discussed in previous section. Based on these analyses, the formation temperature of  $\beta\text{-In}_2\text{Se}_3$  was assumed to  $350^\circ\text{C}$  in our system.

### ***4-3. Cu-In-Se phase***

In previous sections, the formation temperature of  $\text{Cu}_{2-x}\text{Se}$  and  $\beta\text{-In}_2\text{Se}_3$  was determined to  $250^\circ\text{C}$  and  $350^\circ\text{C}$ , respectively. In our research, the quality of CIGS absorber is strongly related to the annealing profile during selenization process. Therefore, one- or two-step annealing process was utilized to fabricate CIS/CIGS absorbers in several reports. In order to understand the influence of various annealing profile in detail, we prepared a SLG/Cu/In/Se precursor and annealed it at various temperatures from  $250^\circ\text{C}$  to  $550^\circ\text{C}$  for 30min. The percentages corresponded to fractions of the total thicknesses of Cu, In and Se layers of 0.2, 0.3 and 5.0  $\mu\text{m}$ , respectively. Fig. 4-6 shows the cross-sectional SEM images of  $250^\circ\text{C}$ ,  $350^\circ\text{C}$ ,  $450^\circ\text{C}$ , and  $550^\circ\text{C}$  annealing temperatures. From visual estimation, the grain size was getting larger when the annealing temperature was increasing. On the other hand, we can see there was an uncontinuous phase as a defect in between the bottom of the film and SLG substrate, as shown in Figs. 4-6(a), (b), (c), and (d). We suggested that was due to the Cu-In alloys without completely reacting with Se. When the temperature was increased, the defect was hard to observe but remaining in the film. As we estimated, this was the issue for poor adhesion and binary compounds in the film. This estimation of incomplete selenization made verification by the cross-sectional EDS analyses. As shown in Table 4-3, Se composition detected at the bottom of the film was lower than that near the top.



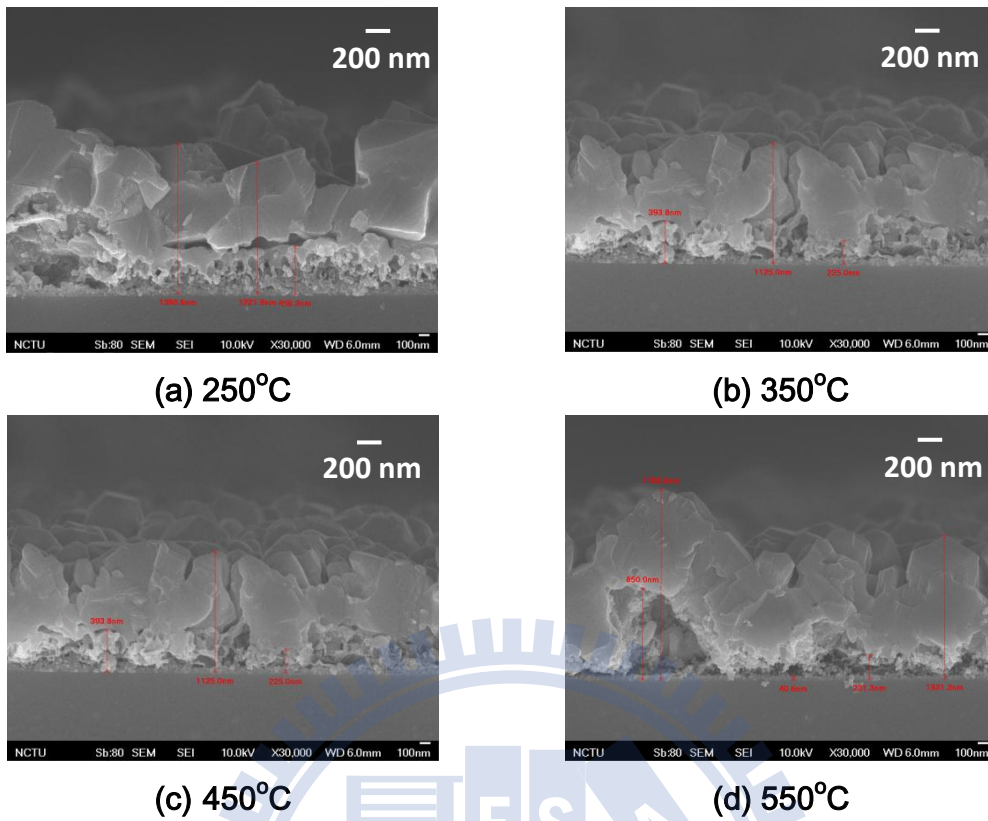


Fig. 4-6 The SEM cross-section of Cu-In-Se annealed at (a) 250°C, (b) 350°C, (c) 450°C, and (d) 550°C.

Table 4-3 Cu-In-Se cross-EDS results.

<i>Temperature</i> (°C)	<i>Se(%)</i>	
	<i>Top</i>	<i>bottom</i>
<i>250</i>	<i>42.12</i>	<i>32.09</i>
<i>350</i>	<i>43.72</i>	<i>35.08</i>
<i>450</i>	<i>45.8</i>	<i>37.6</i>
<i>550</i>	<i>41.88</i>	<i>31.63</i>

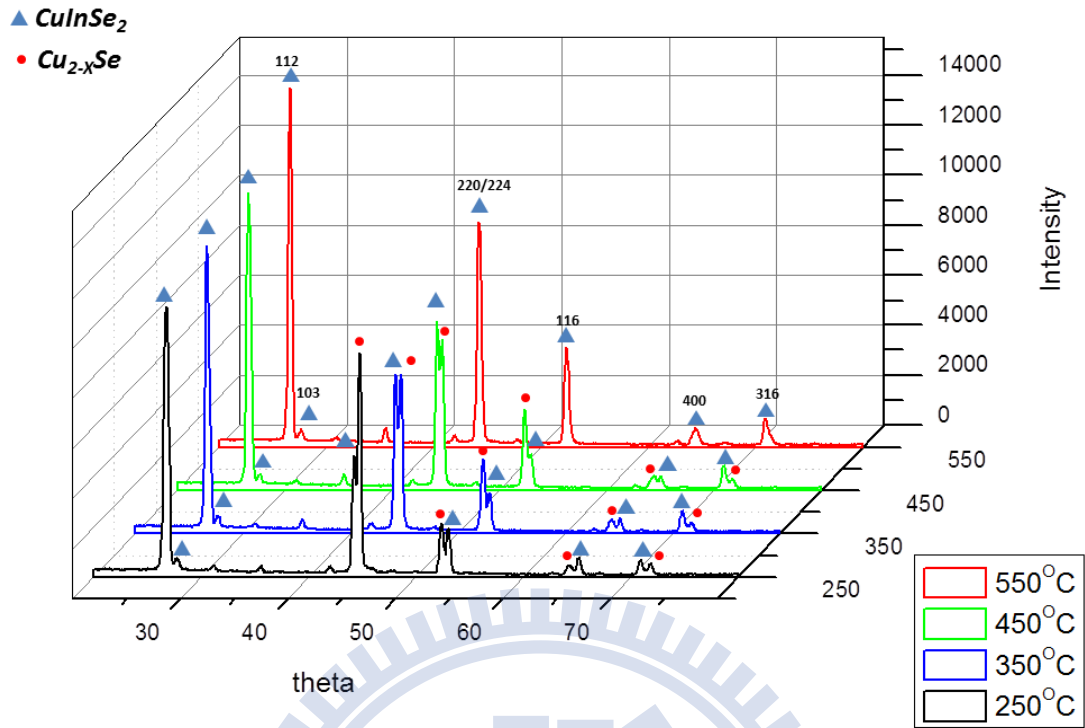


Fig. 4-7 Cu-In-Se XRD annealed in different temperature.

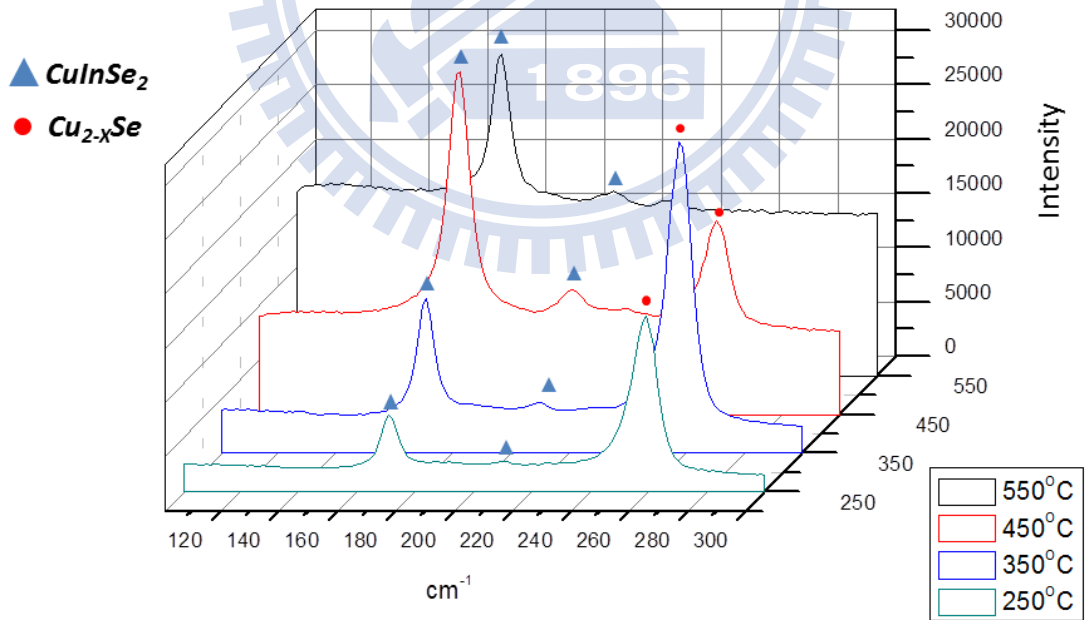


Fig. 4-8 Cu-In-Se Raman annealed in different temperature.



On the other hand, the Se composition of 37.6% at the sample annealed at 450°C was the closest to top compositions, which means the best selenization quality among all samples. However, the bottom Se composition of Sample 550°C was significantly lower than that of Sample 450°C. The reason will be discussed in the following, after the discussions of Raman and XRD results.

The XRD analysis and Raman shift of the one-step annealing samples are shown in the Figs. 4-7 and 4-8 [30-32]. The results revealed that the  $\text{Cu}_{2-x}\text{Se}$  binary phase was segregated at the samples annealed at 250°C, 350°C, and 450°C. While the annealing temperature was elevated to 550°C, both XRD and Raman analyses revealed clearly chalcopyrite and single  $\text{CuInSe}_2$  phase. Moreover, the sample annealed at 550°C showed larger grain size than that at other samples, as shown in Fig. 4-6. However, the Se composition of 31.63% near the bottom of CIS film annealed at 550°C was poor than that of other samples. We predicted that the vertical diffusion of Se might be reduced by the formation of large-grained CIS film, especially at the sample annealed at 550°C. As other research mentioned, the melting point of the  $\text{Cu}_{2-x}\text{Se}$  phase is about 523°C; meanwhile, the liquid  $\text{Cu}_{2-x}\text{Se}$  will diffuse along the boundaries of small-grained CIS crystals and diminish the boundaries of CIS film when the annealing temperature is elevated to over 523°C [15]. Thus, the grain size will be enlarged in the CIS film of 550°C annealing temperature, as well as the Se will be blocked due to diminished boundaries. Therefore, the annealing

temperature between 450°C and 550°C is sensitive and strongly influenced the selenization of CIS absorber. Based on those results, we obtained the method to complete the selenization process, the two-step annealing method. The first-step annealing is to complete the reaction of Cu and In to Se, and the second-step annealing is to further enhance the grain size of chalcogenic CIS film.

#### 4-4. Growing paths determination

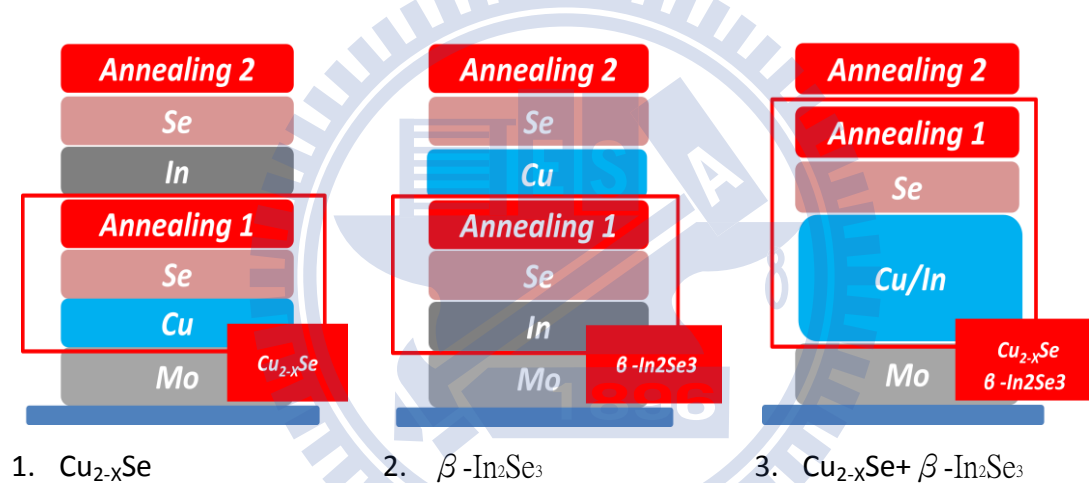


Fig. 4-9 Schematic deposition procedures with different case; (1)  $\text{Cu}_{2-x}\text{Se}$ , (2)  $\beta\text{-In}_2\text{Se}_3$ , and (3)  $\text{Cu}_{2-x}\text{Se} + \beta\text{-In}_2\text{Se}_3$ .

On the basis of these results, three growing paths to form CIS film were designed and processed to confirm the selenization process, as shown in the Fig. 4-9. Detailed expressions of these procedures were discussed below.

- In path 1,  $\text{Cu}_{2-x}\text{Se}$  film was formed by selenizing Cu precursor at the first stage annealing of 250°C. In-Cu alloys and Se were then deposited on the annealed film, and selenized for the second stage at 550°C  $T_{\text{anne}}$  to form

Sample 1.

- In path 2,  $\beta$ - $\text{In}_2\text{Se}_3$  film was formed by selenizing In-Se precursors at the first stage  $T_{\text{anne}}$  of  $350^\circ\text{C}$ . Cu alloys and Se were deposited on the annealed film, and subsequently selenized for the second stage at  $550^\circ\text{C}$   $T_{\text{anne}}$  to form Sample 2.
- In path 3, the interphase composed of  $\text{Cu}_{2-x}\text{Se}$  and  $\beta$ - $\text{In}_2\text{Se}_3$  was formed by selenizing In-Cu-Se precursors at the first stage annealing of  $350^\circ\text{C}$ , and then recrystallized for the second stage at  $550^\circ\text{C}$   $T_{\text{anne}}$  to form Sample 3.

The percentages corresponded to fractions of the total thicknesses of Cu, In and Se layers of 0.2, 0.3 and  $5.0 \mu\text{m}$ , respectively. SEM plane-view micrographs of CIS films are shown in Fig. 4-10. Non-uniform morphology on the CIS film in Sample 1 was possibly due to the aggregation of deposited In, while uniform surface obtained in Samples 2 and 3. Nevertheless, smooth and dense crystallization CIS film was observed in Sample 3. XRD patterns shown in Fig. 4-11(a) reveal that all CIS films are in (112)-oriented crystallization. The Raman peak at  $260\text{cm}^{-1}$  in Sample 2 was attributed to the presence of  $\text{Cu}_{2-x}\text{Se}$  phase, shown in Fig. 4-11(b) [32]. An excess of  $\text{Cu}_{2-x}\text{Se}$  resulted in comparatively uniform surface and large grain size of CIS films in Sample 2 than Sample 1. Nevertheless,  $\text{Cu}_{2-x}\text{Se}$  on top of the CIS-based films result in low device efficiency due to its low resistivity [33].

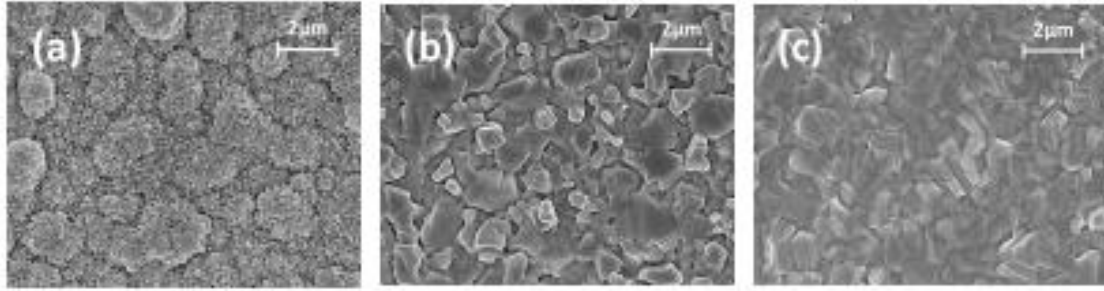


Fig. 4-10 SEM micrographs of CIS films prepared with (a) path 1, (b) path 2, and (c) path 3.

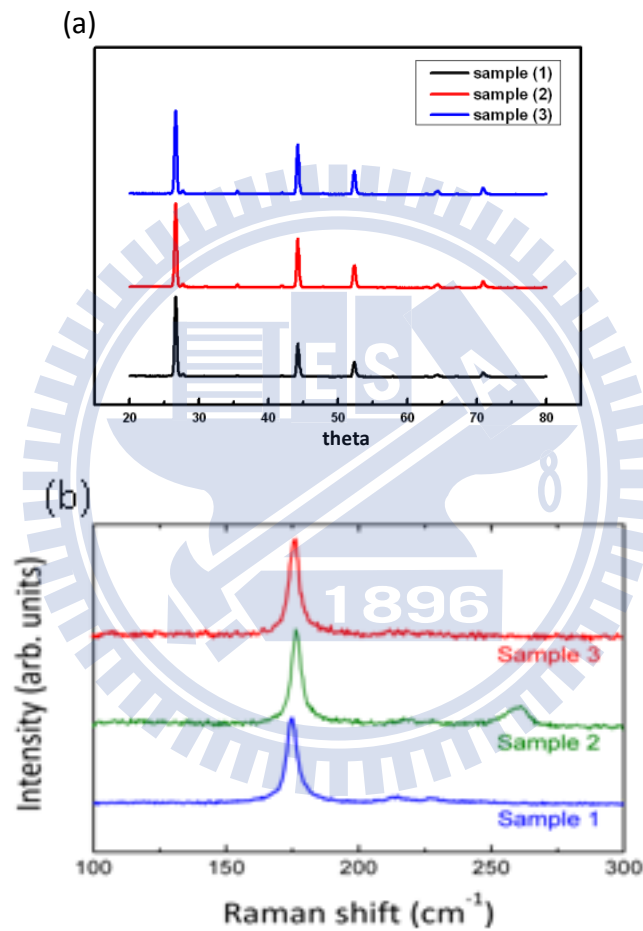


Fig. 4-11 (a) XRD scans and (b) Raman spectra of CIS films selenized with three paths.

On the other hand, XRD analysis revealed that higher ratio of (220/204) to (112)-orientation CIS film was obtained in Sample 3 compared to Samples 1 and 2, as shown in Fig. 4-11(a). Several reports concluded preferred

(220/204)-oriented CIS film benefits device efficiency. In summary, CIS films fabricated by the path 1 ( $\text{Cu}_{2-x}\text{Se}$ ) showed poor roughness and small grain size, while films by the path 2 ( $\beta\text{-In}_2\text{Se}_3$ ) revealed the presence of unexpected  $\text{Cu}_{2-x}\text{Se}$  phase. In contrast, path 3 ( $\text{Cu}_{2-x}\text{Se}/\beta\text{-In}_2\text{Se}_3$ ) shows the better ratio of (220/204) to (112)-orientation, uniform, and dense crystallization in phase. Therefore, we preferred the path 3 for the selenization process to form the CIS films; meanwhile, the structure of SLG/Cu-In/Se precursors and two-step annealing process were selected as the primary formation method in this research.

#### ***4-5. Cu-In-Ga-Se phase***

In previous sections, the procedures and parameters were determined to form single-phase CIS absorber. For the formation of CIGS absorbers, Cu/Ga target was utilized instead of the Cu target. In general, the formation mechanism of CIGS is roughly similar to that of CIS absorbers. Based on above results, we selected co-sputtering deposition for Cu-In-Ga precursors by Cu/Ga and In targets. Co-sputtering not only can provide smooth precursors but also avoid the aggregation of In in surface morphology. The percentages corresponded to fractions of the total thicknesses of Cu-Ga, In and Se layers of 0.26, 0.30 and 5.6  $\mu\text{m}$ , respectively. Besides, the growing path consists of the SLG/Cu-In/Se precursors and two-step annealing was selected as our formation method.

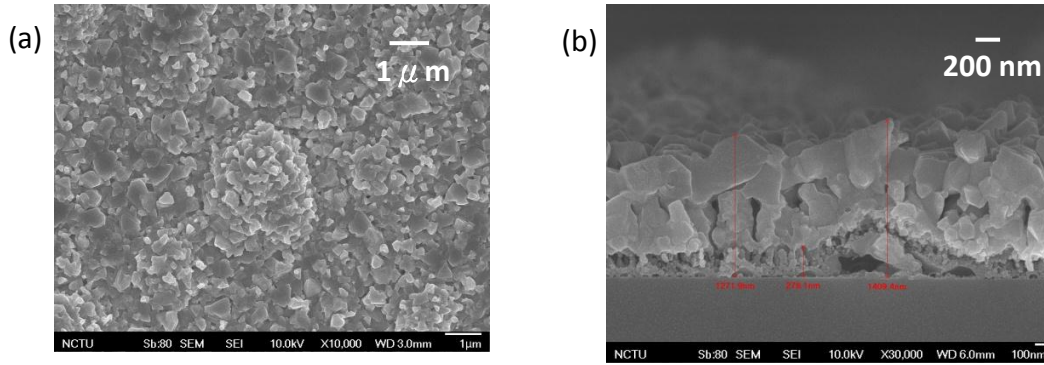
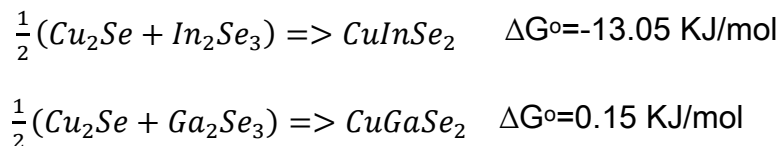


**Fig. 4-12 SEM micrographs of CIGS prepared with path 3 by co-sputtering (a) Top-view and (b) cross-section.**

In the beginning of our process for CIGS absorbers, the annealing temperature was set as 350°C and 550°C, as a two-step annealing procedure. The SEM images of CIGS film are shown in Fig. 4-12. The CIGS absorber revealed small grains, poor selenization near the bottom of film, as well as an adhesion issue to the substrate, as shown in Fig. 4-12(b). We suggested that the formation speed of Cu-In-Se is much faster than that of Cu-Ga-Se compounds, and the CIS phase will be a barrier to Se diffusion. Table 4-4 is the standard free energies ( $G^\circ$ ) for related compounds, and the  $\Delta G^\circ$  of CIS and CGS reactions is listed below [34]:



The  $\Delta G^\circ$  of CIS formation is lower than that of CGS phase [34]. It is also in good agreement with our suggestion that the CIS phase will be formed first, and be the barrier inside the film. Therefore, we modified a new annealing profile for CIGS absorbers. From the views of the Cu-In-Se phase, 450°C was

the optimized annealing temperature with relatively complete selenization, as shown in Table 4-3. Thus, the two-step annealing was upgraded to three-step annealing profile, including 350°C, 450°C, and 550°C annealing temperatures.

**Table 4-4 Standard Free Energies , $G^\circ$ , of Some Compounds Relevant to the Mo/CIGS/CdS/ZnO System [34].**

compound	$G^\circ$ (298 K), kJ/mol	ref
CdO	-274.7	153
CdS	-176.8	153
CdSe	-170.7	153
CdIn <sub>2</sub> Se <sub>4</sub>	<-557.1	
CdIn <sub>6</sub> Se <sub>10</sub>	<-1329.9	
Cu <sub>2</sub> O	-198.2	153
Cu <sub>2</sub> S	-115.6	153
Cu <sub>2</sub> Se	-103.9	153
CuInSe <sub>2</sub>	<-245	
CuInS <sub>2</sub>	<-260	
CuGaSe <sub>2</sub>	<-283	
CuO	-168.8	153
CuS	-73.6	153
CuSe	-65.2	153
Cu <sup>0</sup>	-10.0	153
Ga <sub>2</sub> O <sub>3</sub>	-1114.4	153
Ga <sub>2</sub> S <sub>3</sub>	-558.7	153
Ga <sub>2</sub> Se <sub>3</sub>	-462.4	153
Ga <sup>0</sup>	-12.2	153
In <sub>2</sub> O <sub>3</sub>	-957.0	153
In <sub>2</sub> S <sub>3</sub>	-404.4	153
In <sub>2</sub> Se <sub>3</sub>	-360	154
In <sup>0</sup>	-17.2	153
MoSe <sub>2</sub>	-180.2	153
Mo <sup>0</sup>	-8.5	153
ZnO	-363.6	153
ZnS	-222.2	153
ZnSe	-193.5	153

<sup>a</sup> The standard enthalpies of formation of the elements are taken at 25 °C, 1 bar, and their entropies at 0 K are set to zero.

## 4-6. Three step process

For the examination of three-step process for CIGS, Raman spectrum was utilized to characterize the phase in the endpoint of every step, shown in Fig. 4-13. The Raman shift represents the phase of (In,Ga)<sub>x</sub>Se<sub>y</sub> and Cu<sub>2-x</sub>Se binary selenides at the peak of 211cm<sup>-1</sup> and 260cm<sup>-1</sup>, respectively, as well as

chalcogenic CIS is at  $174\text{cm}^{-1}$ , as shown in Fig. 4-13(a) [32]. The result of  $350^\circ\text{C}$  and  $450^\circ\text{C}$  annealing temperatures revealed the presence of CIGS,  $\text{Cu}_{2-x}\text{Se}$ , and small amounts of  $(\text{In,Ga})_2\text{Se}_3$  phases. For the result of  $450^\circ\text{C}$  annealing temperature, as shown in Fig. 3-13(b), the Raman shift revealed that the peak at  $176\text{cm}^{-1}$  increases and the peaks of  $\text{Cu}_{2-x}\text{Se}$  decreases. The Raman shift at  $176\text{cm}^{-1}$  represents the formation of CIGS phase, which is attributed to the re-crystallization of  $\text{Cu}_{2-x}\text{Se}$ ,  $(\text{In,Ga})_2\text{Se}_3$ , and CIS phase at the annealing temperature above  $375^\circ\text{C}$ . The optimization of the annealing temperature is required to complete the chalcopyrite formation without film delamination. At the third step, the film was further annealed at  $550^\circ\text{C}$  to eliminate the binary selenides, as well as improve the crystallization of CIGS phase. As shown in Fig. 4-13(c), Raman shift shows that the film was chalcopyrite CIGS phase with the exclusion of binary selenides. Therefore, the annealing temperature of selenization process should be reasonably selected to make complete reaction and yield good adhesion of CIGS film to the Mo-coated substrate. On the other hand, the XRD analysis of the CIGS film fabricated by three-step process exhibited the peak of 220/204-orientation approximately equals to that of 112-orientation, as shown in Fig. 4-14. We suggested that the enhancement of 220/204-orientation was attributed to the extra temperature of  $450^\circ\text{C}$ , as we mentioned above. We annealed the SLG/Cu-Ga/In/Se precursors at temperatures of  $350^\circ\text{C}$ ,  $450^\circ\text{C}$  and  $550^\circ\text{C}$  for



60, 30, and 30 min, respectively. SEM images of the CIGS films with three-step annealing processes are shown in Figs. 4-15(a) and (b). Top-view SEM micrograph depicted that the precursor film was smooth and densely packed in surface morphology, as shown in Fig. 4-15(a). Fig. 4-15(b) revealed that the CIGS film with three-step annealing was small-grained at the interface to the Mo layer. Top view EDS analyses of the Cu-Ga-In precursor and selenized CIGS film are shown in Table 4-5. The Ga/(In+Ga) ratio of the precursor and three-step annealed CIGS film was 0.196 and 0.056, respectively. It showed that the Ga/(In+Ga) ratio of the selenized film was slightly less than that of the precursor film. Cross-sectional EDS analyses, including top, middle, and bottom measuring points of CIGS films, are shown in Table 4-6. The Ga/(In+Ga) ratio of both selenized films was arising from surface (Top point) to bottom of CIGS film (Bottom point). It presumably attributed to the accumulation effect of Ga at the bottom of CIGS film after annealing, as well as resulted in secondary layer and small-grained crystallization near back contact film, shown in Fig. 4-15(b). We assumed that CGS phase was segregated near the bottom of the film, and resulted in non-uniform distribution of elementary composition; meanwhile the surface of the film was getting more Cu and less Ga elements than that at the bottom. It indicated that the  $\text{Cu}_{2-x}\text{Se}$  and CIS were formed at the surface of the film. The CIS with lower band gap of 1.02eV will reduce  $V_{oc}$ , and  $\text{Cu}_{2-x}\text{Se}$  on the surface of the absorber will reduce the fill factor and decrease the cell

efficiency.

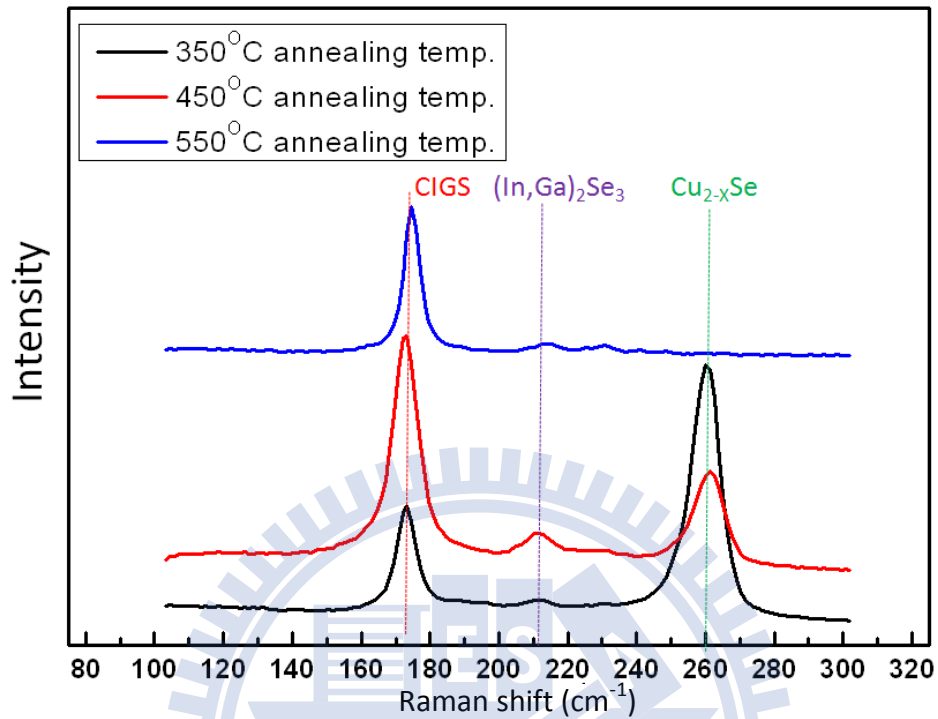


Fig. 4-13 Raman scans of three-step annealing CIGS films annealed of (a) 350°C, (b) 450°C, and (c) 550°C.

Table 4-5 Top view EDS analyses.

Sample	Annealing temp.	Cu/(In+Ga)	Ga/(In+Ga)
CuGaIn Precursor film	-	1.12	0.196
Three-step annealed CIGS film	350°C/450°C/550°C	1.19	0.056

Table 4-6 cross-view EDS analyses for three step annealing.

Point	Cu	In	Ga	Se	Ga/(In+Ga)
Top	33.56	17.69	0.86	47.89	0.05
Middle	19.05	16.07	13	51.88	0.45
Bottom	18.26	10	26.02	45.64	0.72

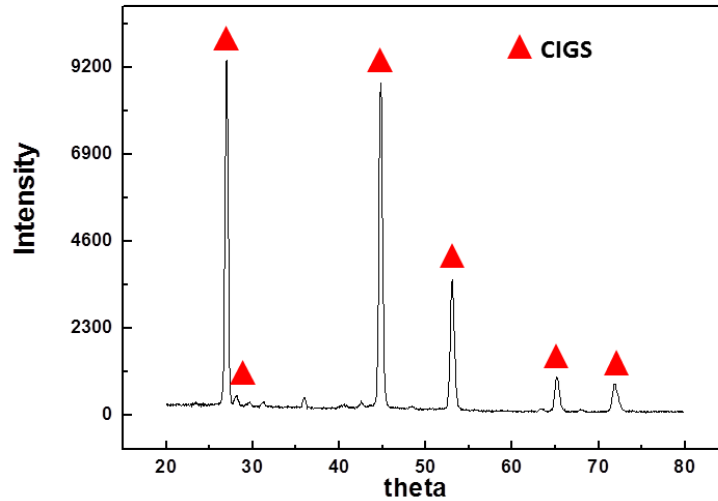


Fig 4-14 XRD of the three step processed CIGS.

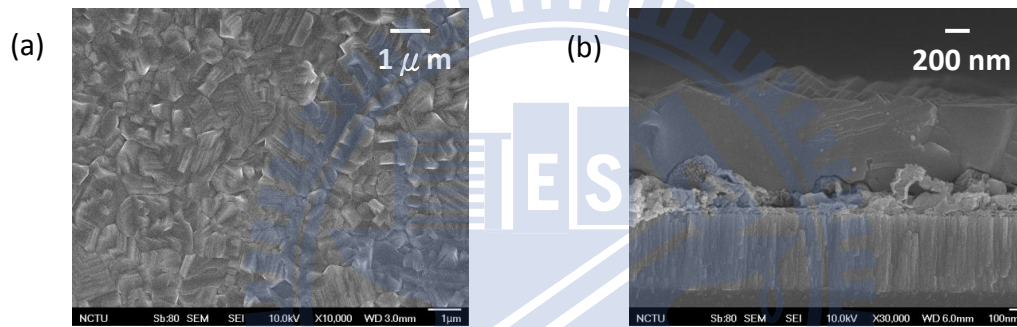


Fig. 4-15 SEM micrographs of CIGS prepared with three three step process (a) Top-view and (b) cross-section.



Fig. 4-16 The modified structure.

To solve the accumulation of Ga in the bottom of absorbers, a specific structure of precursors was studied. Fig. 4-16 shows the schematic explanation for the structure. After annealing process, the top-view EDS result of this structure showed roughly equal Ga/(In+Ga) ratio to that of its precursors, as listed in Table 4-7. In comparison, the specific structure showed high

Ga/(In+Ga) of about 0.18, which was much higher than 0.056 of the SLG/Cu-Ga-In/Se structure. On the other hand, the cross-sectional EDS analysis showed more than 0.3 of Ga/(In+Ga) ratio at both top and bottom of the film, as shown in Table 4-8. The SEM images are shown in Fig. 4-17. The cross-sectional SEM image shows the periodic small-grained structure at both middle and bottom of the film. This situation was referred to the small amounts of Ga accumulated on first-deposited Se. Therefore, we suggested the pre-mixture of Se in the precursors might be a barrier to prevent serious diffusion of Ga. To mix small amounts of Se with Cu-Ga-In precursors before three-step annealing, we proposed a pre-heating treatment. The details will be introduced and examined in the next section.

**Table 4-7 Top view EDS analyses.**

Sample	Annealing temp.	Cu/(In+Ga)	Ga/(In+Ga)
CuGaIn Precursor film	-	1.12	0.196
Ga solution	350°C/450°C/550°C	1.19	0.18

**Table 4-8 cross section view EDS analyses for Ga solution.**

Point	Cu	In	Ga	Se	Ga/(In+Ga)
Top	28.4	16.99	8.23	46.38	0.32
Middle	28.16	17.71	6.03	48.11	0.25
bottom	17.5	14.42	6.61	61.47	0.31

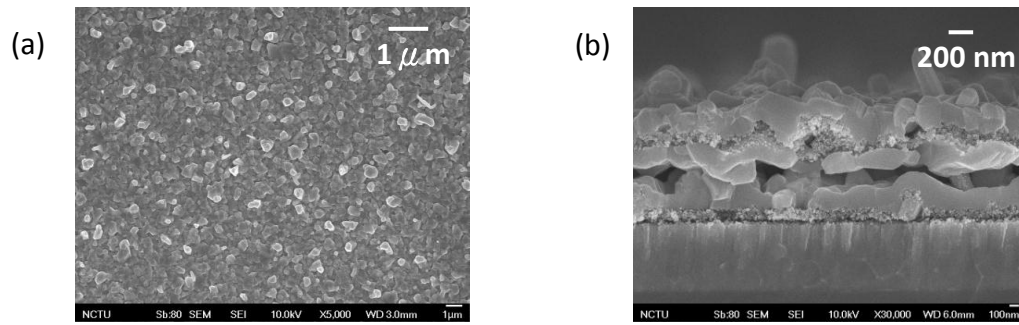


Fig. 4-17 SEM micrographs of CIGS prepared with Ga solution (a) Top-view and (b) cross-section

#### ***4-7. Four step process***

As we discussed above, the pre-mixture of Se in the Cu-Ga-In precursor film probably benefits the uniformity of elementary distribution. Thus, we proposed a four-step annealing process consisting of pre-heating treatment and followed annealing at elevated temperatures to improve the depth-profiled Ga distribution of CIGS films. The four-step annealing process consists of pre-heating treatment and subsequently three-step annealing. The pre-heating treatment indicates that the Cu-Ga-In/Se stacked layer is annealed at 125°C for 15 min first. By this treatment, selenium is expected to diffuse into the Cu-Ga-In precursor film, i.e., homogenized Cu-In-Ga-Se film is obtained. The following three steps are the same as the three-step annealing process. The pre-heating of the sputtered Cu-Ga-In and evaporated Se film was utilized to mitigate adhesion and Ga accumulation problems in the formation of CIGS film. The optimized temperature of the preheating procedure was 125°C, followed annealing at temperatures of 350°C, 450°C, and 550°C respectively. The morphology and compositional analyses of the CIGS film by three- and

four-step annealing processes were examined and discussed. EDS analysis of precursor film indicated the composition of  $\text{Cu}/(\text{Ga}+\text{In}) = 1.12$  and  $\text{Ga}/(\text{In}+\text{Ga}) = 0.196$ . Cross-sectional SEM image shown in Fig. 4-18(a) revealed that the CIGS film with three-step annealing was small-grained at the interface with the Mo layer. However, the film with four-step annealing depicted uniform, large-grained, and without delamination of CIGS film in cross-sectional SEM image, shown in Fig. 4-18(b).



**Fig. 4-18** Cross-sectional SEM micrographs of CIGS films with (a) three-step and (b) four-step annealing process.

Top view EDS analyses of the Cu-Ga-In precursor and selenized CIGS films are shown in Table 4-9. The  $\text{Ga}/(\text{In}+\text{Ga})$  of precursor, three-step and four-step annealed CIGS films were 0.196, 0.056, and 0.123, respectively. This result indicated that the  $\text{Ga}/(\text{In}+\text{Ga})$  ratio of annealed films was slightly less than that of precursor film. Cross-sectional EDS analyses, including top, middle, and bottom measuring points of CIGS films, were shown in Table 4-10. The  $\text{Ga}/(\text{In}+\text{Ga})$  ratio of both selenized films was arising from surface (Top point) to bottom of CIGS film (Bottom point). It is presumably attributed to the accumulation effect of Ga at the bottom of CIGS film after annealing, as well

as resulted in secondary layer and small-grained crystallization near back contact film, shown in Fig. 4-18(a). Fig. 4-19 shows the trend of Ga/(In+Ga) ratio from top to bottom of the resulting films. It revealed that the CIGS film with four-step annealing process could mitigate the Ga accumulation problem obviously. The estimated band diagram of three- and four-step processes are shown in Fig. 4-20. The slightly high Ga accumulation at the bottom of absorber film benefits the band gap tailoring such as a built-in back surface field (BSF), as shown in Fig.4-20 (b) [38]. On the other hand, the lack of Ga on the absorber surface subsequently yields low Voc and limits the cell efficiency [38]. The CIGS film with pre-heating treatment and four-step annealing process can mitigate the Ga accumulation, eliminate the delamination of resulting film, and modify the distribution of Ga/(In+Ga) ratio. Consequently, demonstrated CIGS absorber film is feasible to achieve high Voc and high conversion efficiency [38].

**Table 4-9 Top view EDS analyses.**

Sample	Annealing temp.	Cu/(In+Ga)	Ga/(In+Ga)
CuGaIn Precursor film	-	1.12	0.196
Three-step annealed CIGS film	350°C/450°C/550°C	1.19	0.056
Four-step annealed CIGS film	125°C/350°C/450°C/550°C	1	0.123

**Table 4-10 Cross-sectional EDS analyses [Ga/(In+Ga) ratio].**

Sample	Ga/(In+Ga)		
	Top	Middle	Bottom
Three-step annealed CIGS film	0.046	0.45	0.72
Four-step annealed CIGS film	0.10	0.17	0.32

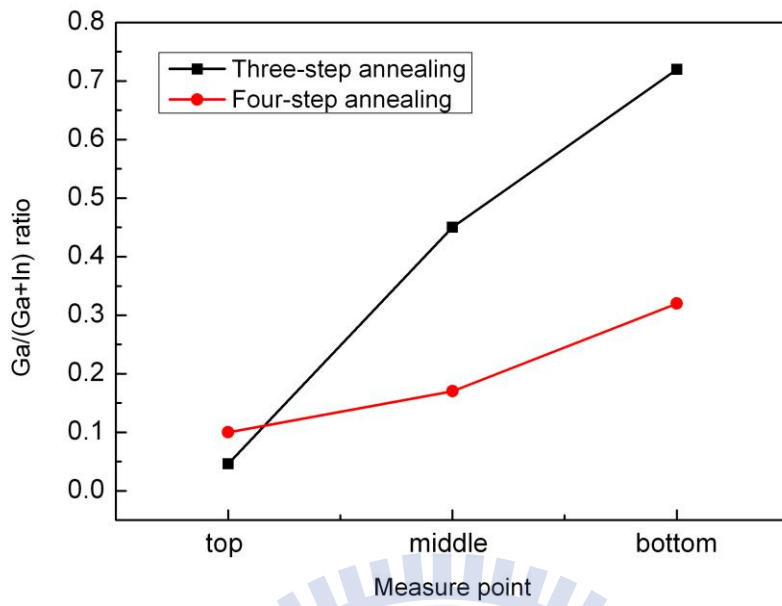


Fig. 4-19 Depth-profiled Ga/(In+Ga) ratio through the bulk of CIGS film prepared by three- and four-step annealing processes.

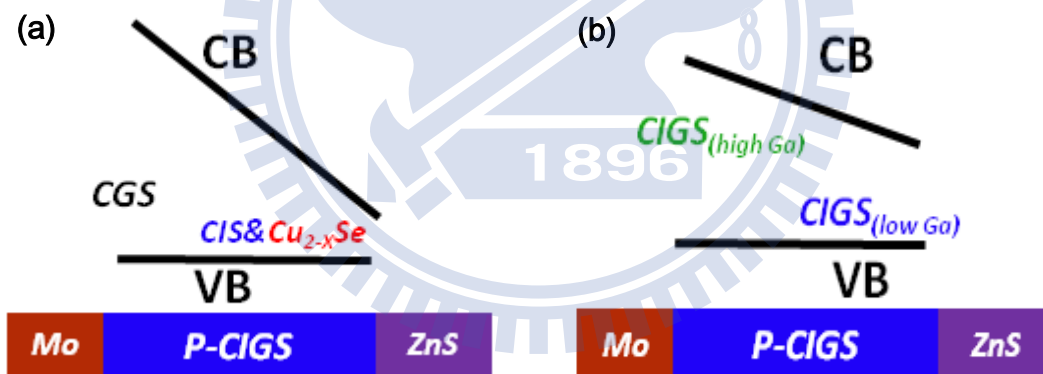


Fig. 4-20 The band diagram of (a) three- and (b) four-step processes.



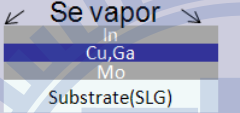
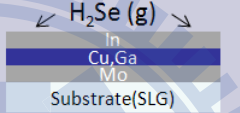
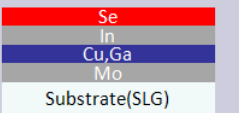
## ***4-8. Comparison***

The accumulation of Ga in the bottom side of the CIGS film is a critical issue in film growth, and strongly affects the efficiency of the device. In this study, a four-step annealing (Solution B) was introduced and examined to overcome this issue. On the other hand, a mixture of  $\text{H}_2\text{Se}_{(g)}$  and  $\text{Ar}_{(g)}$  was utilized to be the reactant while selenization (Solution A), which can also mitigate the accumulation of Ga [36]. In Table 4-11, the comparison of the two methods is listed. The top-view EDS analyses of Ga/In+Ga ratios (Ga%) were characterized to identify the depth-profiled Ga distribution. In other research, the conventional process to form a CIGS absorber made a result that the Ga% of Cu-In-Ga precursors and resulting CIGS was 20% and 5%, respectively [35]. It represents that Ga will diffuse to the bottom side after annealing process in a Se vapor environment. The result of the process by using the mixture of  $\text{H}_2\text{Se}_{(g)}$  and  $\text{Ar}_{(g)}$  reveals that the Ga% of the CIGS film was raised to about 13%, while 2% was obtained in conventional selenization without Ar treatment, shown in Table 4-10. On the other hand, by using four-step annealing method, the Ga% was about 13% as well as was 5% by three-step annealing.

The Ga% of resulting CIGS film was successfully improved by using of the mixture of  $\text{H}_2\text{Se}$  and Ar, or four-step annealing method alternatively [36].

Compared with the using of the mixture of H<sub>2</sub>Se and Ar, the four-step annealing not only improved the depth-profiled Ga distribution but also avoided the toxic H<sub>2</sub>Se. In other words, proposed four-step annealing is a safe process, which can improve the quality of CIGS absorbers.

**Table 4-11 Comparisons of two methods**

Process	Conventional selenization (Se vapor)	Solution A (mixture of H <sub>2</sub> Se and Ar)	Solution B Proposed four-step annealing
Cu-In-Ga (Cu-In-Ga/Se) precursor structure			
Ga/(In+Ga) ratio of Cu-In-Ga precursors (EDS)	20%	20%	19%
Ga/(In+Ga) ratio of selenized CIGS (EDS)	5%	2%	5% (three-step annealing)
Modified methods		H <sub>2</sub> Se <sub>(g)</sub> +Ar <sub>(g)</sub>	Four-step annealing
Ga/(In+Ga) ratio of resulting CIGS after modification		13%	13%
Reference	Solar Energy Materials, vol. 42, pp. 271-279, 1996. [35]	2009 34 <sup>th</sup> PVSC pp. 000844-000847 [36]	IPC 2011: I-SA-VIII 8-3 [37]

# Chapter 5

## Conclusions and future works

### *5-1. Conclusions*

Both CIS and CIGS absorber films have been prepared and studied. The modified fabrication process, including sputtered precursors and subsequent selenization procedure, was discussed. The investigation of  $\text{Cu}_{2-x}\text{Se}$  and  $\beta$ - $\text{In}_2\text{Se}_3$  binary films was firstly carried out to determine the growing mechanism of CIS films. The results concluded that path 3 ( $\text{Cu}_{2-x}\text{Se}$  and  $\beta$ - $\text{In}_2\text{Se}_3$ ) is comparatively suitable for the formation of CIS films; meanwhile, the SLG/Cu-Ga-In/Se structure was utilized for precursors. For the selenization, the annealing temperature of  $450^\circ\text{C}$  was studied to improve the selenization quality near the bottom of absorbers. Thus, a modified three-step annealing was adopted for the formation of absorbers. The resulting film showed enhanced adhesion to Mo-coated SLG substrates and higher 220/204-orientation in phase. Nevertheless, Ga accumulation near bottom of the films was an issue that might reduce the device quality. On the other hand, it also indicated that the  $\text{Cu}_{2-x}\text{Se}$  and CIS were formed at the surface of the film. The CIS with lower band gap of 1.02eV than that of CIGS phase will reduce  $V_{oc}$ , and  $\text{Cu}_{2-x}\text{Se}$  on the surface of the absorber will reduce the fill factor and decrease the cell efficiency.

To solve these issues, a four-step annealing process consisting of

pre-heating treatment and followed annealing at elevated temperatures was proposed to improve the depth-profiled Ga distribution of CIGS films. The CIGS film with the four-step process exhibited more uniform Ga distribution through the bulk of CIGS film and higher Ga concentration near the surface than that without pre-heating treatment. The modified Ga distribution benefits uniform-grained CIGS absorber film without delamination issue. On the other word, the modified fabrication process with respect to the CIGS absorbers might improve the adhesion issue as well as the cell efficiency.

## ***5-2. Future works***

In this study, the four-step annealing process was introduced to mitigate the accumulation phenomenon of Ga, as well as to obtain the CIGS absorbers with normal-gradient band gap. As we mentioned in Section 1-8, slightly graded band gap near the bottom of CIGS will improve carrier-collected efficiency, as a BSF. On the other hand, the band gap near the surface of absorbers we obtained was lower than that at bottom side. To further improve the CIGS absorber, V-shaped Ga distribution is one of the targets to be considered, which is successfully realized by the co-evaporation process but the selenization process. The V-shaped band gap of the CIGS absorber was reported to not only improve the carrier collection, but also enhance Voc in cell performance.

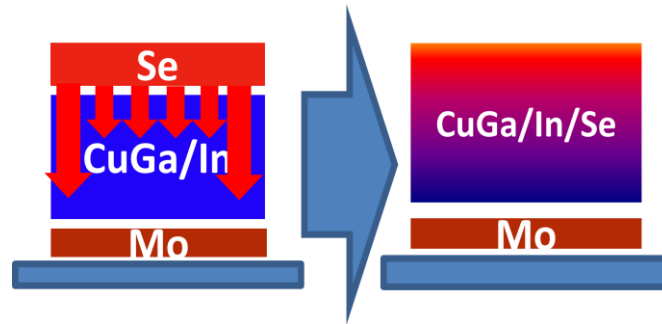


Fig. 5-1 The schematic explanation of the first-step process.

The V-shaped band gap is possibly achieved based on four-step annealing and double-stacked Cu-Ga-In precursors. Firstly, a CIGS absorber with graded band gap as a BSF is coated on the Mo-coated SLG, as shown in Fig. 5-1. The pre-heating treatment is utilized to achieve slightly graded band gap in this procedure. The temperature of pre-heating treatment is sensitive to the resulting film. Second, a highly Ga-doped Cu-Ga-In precursor is deposited on the surface of the CIGS obtained in advance, as shown in Fig. 5-2. After secondary selenization (three-step annealing) and KCN etching, a CIGS with double graded band gap (V-shape) will be obtained. The thickness of double-stacked precursor films must be considered and optimized.

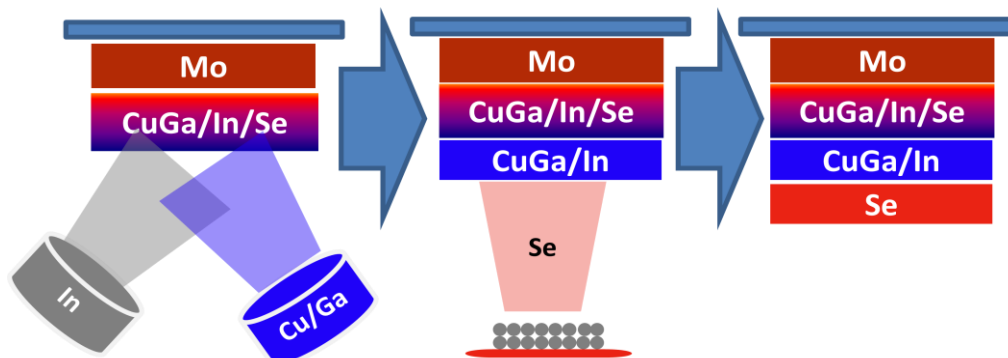
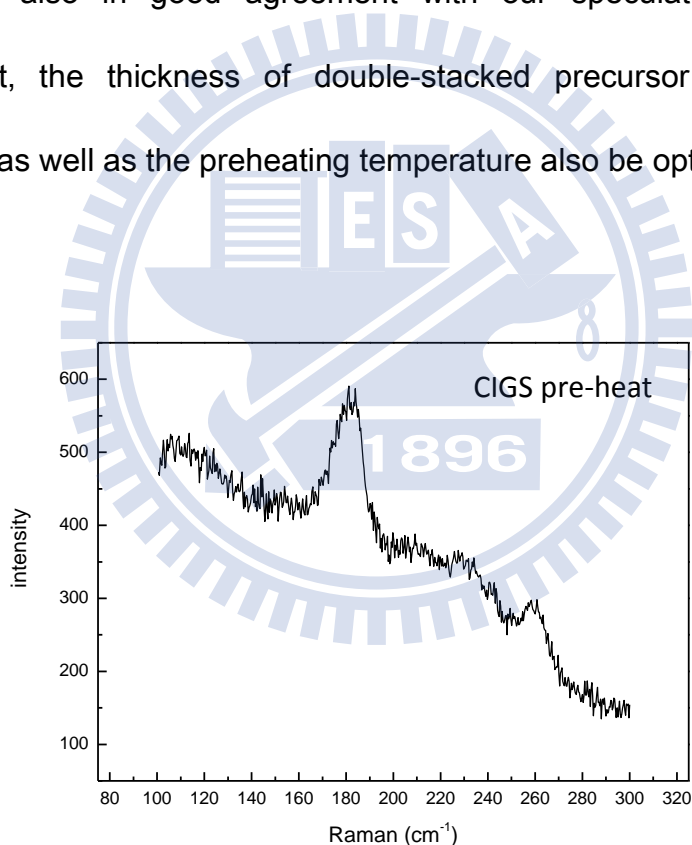


Fig. 5-2 The fabrication process of double-stacked precursors and followed selenization.

We have targeted the V-shaped Ga distribution in CIGS absorbers. Presently, the EDS result revealed that the Ga% of the resulting CIGS film was up to 20% by using the four-step annealing and double-stacked precursors. Nevertheless, the film was peeled off after wet etching process of KCN. We assumed that the presence of  $\text{Cu}_{2-x}\text{Se}$  phase is the cause of peeling. Raman result, shown in Fig. 5-3, revealed that the shift at  $260\text{cm}^{-1}$  represents  $\text{Cu}_{2-x}\text{Se}$  compounds, also in good agreement with our speculation. For further improvement, the thickness of double-stacked precursor films must be considered, as well as the preheating temperature also be optimized.



**Fig.5-3 Raman shift of the CIGS film after the first annealing.**

# References

1. W. G. Adams and R. E. Day, *Proc. Roy. Soc.* **A25**, 1877, p. 113.
2. J. Zhao, A. Wang, M. Green, and F. Ferrazza, *Appl. Phys. Lett.* **73**, 1998, p. 1991.
3. O.Schultz, S. W. Glunz, and G. P. Willeke, *Prog. in Photovoltaics: Research and Applications*.**12**, 2004, p. 553.
4. PARKES, J., TOMLINSON, RD and HAMPSHIRE, MJ, *Journal of Crystal Growth* **20**, 1973, p. 773.
5. A. Rockett, F. Abou-Elfotouh, D. Albin, M. Bode, J. Ermer, R. Klenk, T. Lommasson, T.W.F. Russell, R.D. Tomlinson, J. Tuttle, L. Stolt, T. Walter, T.M. Peterson, *Thin Solid Films* **237**, 1994, p. 1.
6. T. Nakada, D. Iga, H. Ohbo, A. Kunioka *Jpn. J. Appl. Phys.* **36 (No. 2A)**, 1997, p. 732 part 1.
7. K. Orgassa, HW Schock and JH Werner, *Thin Solid Films* **431–432**, 2003, p. 387.
8. S. Mahieu, W. P. Leroy, K. Van Aeken, M. Wolter, J. Colaux, S. Lucas, G. Abadias, P. Matthys, and D. Depla, *Solar Energy* **85**, 2011, p. 538.
9. D. Abou-Ras, G. Kostorz, D. Brémaud, M. Kaelin, F.V. Kurdesau, A.N. Tiwari, M. Döbeli, *Thin Solid Films* **480–481**, 2005, p. 433.
10. U. Rau, A. Jasenek, R. Herberholz, H.-W. Schock, J.-F. Guillemoles, D. Lincot, L. Kronik, *Proc. 2nd World Conf. on Photovoltaics*, 1998, p. 428.
11. J.-F. Guillemoles, U. Rau, L. Kronik, HW Schock and D. Cahen., *Adv.*

- Mater.* **11**, 1999, p. 957.
12. Godecke T., Haalboom T., and Ernst F., *Z Metallkd*, **91**, 2000, p. 622.
  13. T. Haalboom, T. Gödecke, F. Ernst, M. Rühle, R. Herberholz, H.W. Sckhock Beilharz, K.W. Benz, *Inst. Phys. Conf. Ser. No. 152*, 1998, p. 249.
  14. Wada, T., Hayashi, S., Hashimoto, Y., Nishiwaki, S., Sato, T., Negami, T., and Nishitani, M., *Proc.2nd WCPEC*, 1998, p. 403.
  15. S. Nishiwaki, T. Satoh, S. Hayashi, Y. Hashimoto, T. Negami and T. Wada., *J. Mater. Res.***14**, 1999, p. 4514.
  16. R. Herberholz, U. Rau, H.W. Schock, T. Haalboom, T. Gödecke, F. Ernst, C. Beilharz, K.W. Benz, D. Cahen, *Eur. Phys. J. AP***6**, 1999, p. 131.
  17. Cahen, D., *Proc. 7th. Int. Cof Mater. Res. Soc*, 1987, p. 433-442.
  18. M. Burgelman, F. Engelhardt, J.F. Guillemoles, R. Herberholz, M. Igalson, R. Klenk, M. Lampert, T. Meyer, V. Nadenau, A. Niemegeers, J. Parisi, U. Rau, H.W. Schock, M. Schmitt, O. Seifert, T. Walter, S. Zott, *Prog., Photovoltaic. Res. Appl***5**, 1997, p. 121.
  19. Migliorato, P., Shay, J. L., Kasper, H.M., and Wagner, S., *J. Appl. Phys.* **46**, 1975, p. 1777.
  20. Noufi, R., Axton, R., Herrington, C., and Deb, S.K., *Appl Phys. Lett.* **45**, 1984, p. 668.
  21. Herberholz, R., Rau, U., Schock, H.-W., Haalboom, T., Godecke, T., Ernst, F., Beilharz, C., Benz, K.W., and Cahen. D., *Eur. Phys. J. AP* **6**, 1999, p.



- 131.
22. Schmid, D., Ruckh, M., Grunwald F., and Schock, H.-W., *J. Appl. Phys.* **73**, 1993, p. 2902.
23. [http://www.zsw-bw.de/fileadmin/ZSW\\_files/Infoportal/Presseinformationen/docs/pi11-2010-e\\_ZSW-Weltrekord-DS-CIGS.pdf](http://www.zsw-bw.de/fileadmin/ZSW_files/Infoportal/Presseinformationen/docs/pi11-2010-e_ZSW-Weltrekord-DS-CIGS.pdf)
24. Gabor, A.M., Tuttle, J.R., Albin, D.S., Contreras, M.A., Noufi, R., and Hermann, A.M., *Appl. Phys. Lett.* **65**, 1994, p. 198.
25. Gabor, A.M., Tuttle, J.R., Bode, M.H., Franz, A., Tennant, A.L., Contreras, M.A., Noufi, R., Jensen, D.G., and Hermann, A.M., *Solar Energy Mater. Solar Cells* **41**, 1996, p. 247.
26. T. Dullweber, G. Hanna, U. Rau, HW Schock, *Solar Energy Mater. & Solar Cells* **67**, 2001, p. 145.
27. JJM Binsma and HA van der Linden, *Thin Solid Films* **97**, 1982, p. 237.
28. T. L. Chu, Shirley S. Chu, S. C. Lin and J. Yue, *J. Electrochem. Soc.* **131**, 1984, p. 2182.
29. Vijay K. Kapur, Bulent M. Basol, Eric S. Tseng, *Solar Cells* **21**, 1987, p. 65.
30. JCPDS XRD data base.
31. S. Yamanaka, et. Al, *Jpn. J.Appl.Phys.* **30**, 1991, pp. 442.
32. H.K.Song, S.G. Kim, *Solar Cells* **75**, 2003, p. 145.
33. F. Mesa, C.Calderon, *Thin Solid Films* **518**, 2010, p. 1764.
34. Jean-François Guillemoles, *J. Phys. Chem. B* **104**, 2000, p. 4849.

35. N. G. Dhere and K. W. Lynn, *Solar Energy Materials* **42**, 1996, p. 271.
36. W. K. Kim, G. M. Hanket, and W. N. Shafarman, *PVSC 34*, 2009, p. 000844.
37. Chi-Yu Chiang, Yi-Chih Wang, Po-Chuan Tsai, and Han-Ping D. Shieh, *IPC*, 2011, I-SA-VIII 8-3.
38. Yoshihiro Hamakawa, *Thin-Film Solar Cells*, 2003.

